Precambrian deformation belts in compressive tectonic regimes: A numerical perspective

Jonathan Poh, Philippe Yamato, Thibault Duretz, Denis Gapais, Patrick Ledru

To cite this version:

Jonathan Poh, Philippe Yamato, Thibault Duretz, Denis Gapais, Patrick Ledru. Precambrian deformation belts in compressive tectonic regimes: A numerical perspective. Tectonophysics, 2020, 777, pp.228350. 10.1016/j.tecto.2020.228350 . insu-02458916

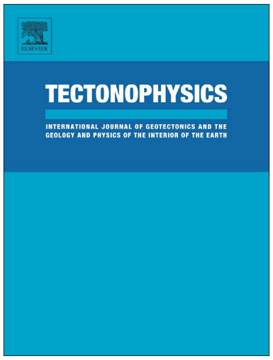

Precambrian deformation belts in compressive tectonic regimes: A numerical perspective

Jonathan Poh, Philippe Yamato, Thibault Duretz, Denis Gapais, Patrick Ledru

PII: S0040-1951(20)30033-0
DOI: https://doi.org/10.1016/j.tecto.2020.228350
Reference: TECTO 228350

To appear in: *Tectonophysics*

Received date: 14 March 2019
Revised date: 10 January 2020
Accepted date: 21 January 2020

Please cite this article as: J. Poh, P. Yamato, T. Duretz, et al., Precambrian deformation belts in compressive tectonic regimes: A numerical perspective, *Tectonophysics*(2020), https://doi.org/10.1016/j.tecto.2020.228350

Precambrian deformation belts in compressive tectonic regimes: A numerical perspective

Jonathan Poh[a,*], Philippe Yamato[a,b], Thibault Duretz[a], Denis Gapais[a],
Patrick Ledru[c]

[a] *Univ Rennes, CNRS, Géosciences Rennes, UMR 6118, 35000 Rennes, France*
[b] *Institut Universitaire de France (IUF)*
[c] *Orano Canada Inc, Saskatoon, Canada*

Abstract

The thermal state of the lithosphere is often considered as the main factor controlling the distribution of the structural and metamorphic features in tectonic systems (ancient versus modern tectonics). Deformation in ancient (weak and hot) lithospheres is distributed whereas deformation in modern (strong and cold) lithospheres is localised into prominent shear zones. The distributed deformation during the Precambrian suggests lower compressive strain rates are required, implying a long compression duration. However, the effects of variable strain rate on the compression of ancient lithospheres remain under-explored. A series of numerical models mimicking Precambrian lithospheric conditions is proposed and a broad range of thermal profiles and shortening rates is tested to investigate their influence on the resultant deformation modes. Two broad deformation styles were found to be significantly influenced by the magnitude of the shortening rates and stand out from the parametric study: (i) pop-downs and upper crustal thrusting at high strain rates that favour the formation of shear zones, and (ii) sedimentary cusping deformation at slower strain rates that generates well-defined vertical finite strain patterns. These two deformation modes were compared with natural examples, providing further insight into the evolution of their respective deformations. The vertical structures at the

---

[*] Corresponding author
Email address: `jonathanpoh87@gmail.com` (Jonathan Poh)

Hearne Craton (western Canadian Shield) could be explained via the sedimentary cusping mechanism by constraining our models with available geological data. Meanwhile, the vertical finite strain patterns from the proposed reference model now provide a tectonic template for future fluid-thermal convection simulations, to predict fluid flow and mineralisation potential.

Keywords: Ancient structures, Precambrian tectonics, Rheology of the lithosphere

---

1. Introduction

Tectonic processes differ over geological times (Fig. 1). This has led to debates on the relevance of tectonic models for specific periods of time (e.g., Bouhallier et al., 1995; Cawood et al., 2006; Condie and Benn, 2013; Gapais et al., 2009; van Haaften and White, 1998; Kranendonk et al., 2004; Turcotte and Schubert, 2002). During the Precambrian, tectonic processes were under the influence of a large geothermal gradients due to the increasing abundance of radiogenic elements within the mantle and continental crust (Condie and Benn, 2013; Turcotte and Schubert, 2002). A hot geothermal gradient implies a low strength of the overlying lithosphere and a weak lithospheric mantle (i.e. 'créme brûlée' model; Brun, 2001; Burov, 2011). Deformation zones generated from hot and mechanically-weak lithospheres can be explained by two tectonic models (Fig. 1A). The first model is pop-down tectonics (Gapais et al., 2014; Gapais, 2018), a mechanism determined from analogue modelling described in Cagnard et al. (2006a). The mechanics of pop-down tectonics highlights the importance of tectonic compression instead of gravitational forces to explain the presence of partially melted sediments, as seen in many Precambrian field examples (see Chardon et al., 2002, 2008; Choukroune et al., 1995; Gapais et al., 2008, 2009; Gapais, 2018). The tectonic structures described in these studies are vertical structures with distributed strains, associated with the downward motions of upper crustal parts and faults, that are limited within the brittle crust. The proposed pop-down mechanism (Fig. 1A) suggests that fluid flow can occur throughout the upper crust and associated structures, making fluid-rock interactions viable for future ore deposition (Gapais et al., 2014; Gapais, 2018). The second tectonic model corresponds to the dome-and-keel model (Fig. 1A, red box). The model relates to structures as those observed in the Mesoarchean East Pilbara Craton (Australia). This structure has spurred on-going debate regarding 'horizontal versus vertical' tectonics (e.g., Bickle et al., 1985; Collins and Vernon, 1991; Kranendonk et al., 2004; Thébaud et al., 2006, 2008; Thébaud and Rey, 2013; François et al., 2014). These structures are composed of large felsic granitic domes (35 – 100 km in diameter) which intruded into a greenstone belt (thick mafic and komatiite volcanic sedimentary rocks). This is described as a 'partial convective overturn' (Collins and Vernon, 1991; Kranendonk et al., 2004). These structures have developed as steeply dipping greenstone sheets and vertical shear zones, inferring potential crustal-scale fluid flow and mineralisation (Thébaud and Rey, 2013).

Tectonic processes inferred in cold and young lithospheres are different compared to tectonic processes inferred in hotter and older lithospheres. These lithospheres are characterised by a decrease of crustal radiogenic heat production and cold geotherms (e.g. Condie and Benn, 2013; Jaupart et al., 2007; Gray and Pysklywec, 2010). Such lithospheres are capable of supporting thicker continental crusts that allow mountain building (Artemieva and Mooney, 2001; Condie and Benn, 2013; Jaupart et al., 2007; Rey and Coltice, 2008). The strength of a lithosphere is controlled by the lithospheric mantle (i.e., 'jelly sandwich model'; Jackson, 2002; Burov, 2011). Deformation zones in cold, mechanically strong, and potentially young lithospheres are often characterised by strain localisation at plate boundaries (Fig. 1B). The shortening of such lithospheres leads to the formation of thrust and nappe systems, subsequent subduction of the continental lithosphere, and mountain building processes (Burov et al., 2006; Burov and Yamato, 2008; Gapais et al., 2009).

There is a consensus on the role played by the thermal state of the lithosphere on the style of orogenic deformation. Geotherms can be used to infer the overall strength of the lithosphere that controls deformation. The strength of the lithosphere has been evaluated at constant strain rates of 10^{-15} s^{-1} (e.g., Burov, 2011). This corresponds to the accepted strain rate for tectonic deformations of up to 10 Ma (Pfiffner and Ramsay, 1982). Geological data from Precambrian orogenic processes suggest that orogenic events have lasted for long periods of time ($>$ 60 Ma in Chardon et al., 2009; Gray and Pysklywec, 2010). This implies that the values of compressive strain rate on old lithospheres are lower than 10^{-15} s^{-1}. However, the effects of variable compressive strain rates on the deformation of ancient lithospheres have remained under-explored.

In this contribution, a series of lithospheric-scaled numerical models have been subjected to a compressive regime to explore a wide range of strain rates and geotherms. The model is constrained by four types of geological observations from a generic Precambrian example: (i) structural evolution, (ii) associated finite strain patterns, (iii) evolution of topography, and (iv) their respective pressure-temperature-time evolution of rocks (i.e., P-T-t paths). Each deformation style is then compared to well known Precambrian field examples, such as the 3.0 Ga Dharwar Craton (India; e.g., Chardon et al., 2009), the 3.5–3.3 Ga East Pilbara Craton (Australia; e.g., François et al., 2014; Thébaud et al., 2006, 2008; Thébaud and Rey, 2013) and the 1.9–1.84 Ga Trans-Hudson Orogen at the Hearne Craton (Canada; e.g., Alexandre et al., 2007; Annesley et al., 2005; St-Onge et al., 2006). The genesis of the vertical structures at the Wollaston-Mudjatik Transition Zone (Hearne Craton) will be then addressed in detail in the discussion. The implications for fluid flow and mineralisation potential will also be discussed.

2. Numerical Approach

2.1. Governing equations

Thermo-mechanical models were used to simulate the shortening of a visco-elasto-plastic continental lithosphere. The two-dimensional (2D) finite-difference, marker-in-cell code (MDoodz; Duretz et al., 2016b) solves the equations of momentum and mass conservation, as well as the heat equation. The linear momentum equation is formulated as:

$$\frac{\partial \tau_{ij}}{\partial x_j} - \frac{\partial P}{\partial x_i} = -\rho^{\mathrm{eff}} g_i, \tag{1}$$

where τ_{ij} and P correspond to the deviatoric stress tensor and total pressure, respectively. The subscript indexes i and j denote the Einstein notation for spatial directions.

Density (ρ) is assumed to be temperature- (T) and pressure- (P) dependent as:

$$\rho = \rho_0^{\mathrm{solid}}(1 - \alpha(T - T_0))(1 + \beta(P - P_0)), \tag{2}$$

where ρ_0^{solid} is the reference density, α is the thermal expansion, and β is the thermal compressibility (see Table 1). T_0 (= 273.15 K), P_0 (= 10^5 Pa), and ρ_0 correspond to reference temperature, pressure, and density, respectively.

The Boussinesq approximation is applied to the models; this approximation assumes that there is negligible thermal expansion and compressibility of crustal and mantle rocks in the absence of phase transformations and neglects volume changes. Mass conservation is ensured by imposing the incompressibility constraint as follows:

$$\frac{\partial v_i}{\partial x_i} = 0, \tag{3}$$

where v_i represents the velocity vector components.

The lithosphere is considered as a Maxwell visco-elasto-plastic medium, which assumes that viscous, plastic, and elastic deformations occur concurrently for a given value of deviatoric stress (τ_{ij}, see also Yamato et al., 2019, for more details). The deviatoric strain rate tensor ($\dot{\varepsilon}_{ij}$) is then formulated as

$$\dot{\varepsilon}_{ij} = \dot{\varepsilon}_{ij}^{\mathrm{vis}} + \dot{\varepsilon}_{ij}^{\mathrm{el}} + \dot{\varepsilon}_{ij}^{\mathrm{pl}}. \tag{4}$$

The effective creep viscosity (η^{eff}) is computed by following a thermally activated power flow law that represents the dislocation creep deformation mechanism (e.g., Chopra and Paterson, 1984; Hansen and Carter, 1983; Ranalli, 1995, 1997). η^{eff} is dependent on the second invariant of the creep strain rate tensor $\dot{\varepsilon}_{\mathrm{II}}^{\mathrm{vis}}$ and is computed as:

$$\eta^{\mathrm{eff}} = \frac{\tau_{\mathrm{II}}}{2\dot{\varepsilon}_{\mathrm{II}}^{\mathrm{vis}}} = F\,A^{-\frac{1}{n}}\,\dot{\varepsilon}_{\mathrm{II}}^{\mathrm{vis}\;\frac{1}{n}-1} \exp\frac{Q}{nRT}\;\exp\frac{aM}{n}, \tag{5}$$

where n, A, and Q are material parameters derived from experiments (see Table 1), $F = \frac{2^{(1-n)/n}}{3^{(n-1)/2n}}$ is the dimension coefficient for triaxial experiments, τ_{II} is the second invariant of the deviatoric stress tensor, $R = 8.314$ J.mol^{-1} is the gas constant, T is the temperature (in K), a is a melt-weakening factor (set to 30), and M is the melt fraction (e.g., Hirth and Kohlstedt, 2004).

Pressure-dependent plasticity is modelled using a Drucker-Prager yield surface, and the yield stress is formulated as follows:

$$\sigma^{\mathrm{yield}} = C\cos\phi + P\sin\phi, \tag{6}$$

where ϕ and C are the friction angle and cohesion, respectively (see Table 1).

The heat equation includes the effect of shear heating (H_S), radiogenic heat production (H_R), latent heat of production or consumption (H_L), and adiabatic heat (H_A).

$$\rho^{\mathrm{eff}} C_{\mathrm{p}}^{\mathrm{eff}} \frac{dT}{dt} = \frac{\partial}{\partial x_i} k \frac{\partial T}{\partial x_i} + H_R + H_S + H_L + H_A, \tag{7}$$

where C_{p} is the specific heat capacity, and k is the thermal conductivity. Shear heating (H_S) is the product of the deviatoric stress and the dissipative part of the strain rate tensor.

$$H_S = (\dot{\varepsilon}_{xx} - \dot{\varepsilon}_{xx}^{\mathrm{el}})\tau_{xx} + (\dot{\varepsilon}_{zz} - \dot{\varepsilon}_{xx}^{\mathrm{el}})\tau_{zz} + 2(\dot{\varepsilon}_{xz} - \dot{\varepsilon}_{xz}^{\mathrm{el}})\tau_{xz} \tag{8}$$

Shear heating (H_S) will be of particular relevance for modelling deep intra-oceanic earthquakes (e.g., Kelemen and Hirth, 2007; McGuire and Beroza, 2012), metamorphic inversion in intra-continental collisions (Duprat-Oualid et al., 2013, 2015; Toussaint et al., 2004), and the localisation and stability of lithospheric scale subduction processes (Burov and Yamato, 2008; Duretz et al., 2015; Thielmann and Kaus, 2012; Liao and Gerya, 2017).

H_L becomes important whenever melting (i.e., partial melting) or crystallisation occurs. In the case of melting, H_L operates as a heat sink ($H_L < 0$), while crystallisation induces a heat source ($H_L > 0$). Partial melting is included as: (i) density with increasing melt fraction, (ii) effective viscosity (see Eqn. 5), and (iii) accounting for the thermal effects of melting/crystallisation. The volumetric fraction of melt is assumed to increase linearly with temperature, according to these relationships (Burg and Gerya, 2005; Gerya and Yuen, 2003):

$$M = 0, \text{at}\, T \leq T_{\text{solidus}}, \tag{9}$$

$$M = \frac{T - T_{\text{solidus}}}{T_{\text{liquidus}} - T_{\text{solidus}}}, \text{at}\, T_{\text{solidus}} < T < T_{\text{liquidus}}, \tag{10}$$

$$M = 1, \text{at}\, T \geq T_{\text{liquidus}}, \tag{11}$$

where T_{solidus} and T_{liquidus} are the wet solidus and dry liquidus temperatures of the considered rock, respectively (see Table 1 for equations). The volumetric fraction of melt (M) influences the effective density (ρ^{eff}) of the partially molten rocks as follows:

$$\rho^{\text{eff}} = \rho \left(1 - M + M \frac{\rho_0^{\text{molten}}}{\rho_0^{\text{solid}}} \right), \tag{12}$$

where $\rho_0^{\text{solid}} = \rho_0$ and ρ_0^{molten} are liquid densities (see Table 1).

Other processes associated with partial melting, such as solid-melt segregation and melt extraction, are neglected because the implementation of two-phase flow beyond the scope of this study. The effect of latent heating due to equilibrium melting or crystallisation is included implicitly by increasing the effective heat capacity ($C_{\mathrm{p}}^{\mathrm{eff}}$) and the thermal expansion (α^{eff}) of the partially crystallised molten rocks ($0 < M < 1$) following Burg and Gerya (2005). Q_L is the latent heat of melting of the considered rocks.

$$C_{\mathrm{p}}^{\mathrm{eff}} = C_{\mathrm{p}} + Q_L \left(\frac{\partial M}{\partial T} \right)_P \tag{13}$$

$$\alpha^{\mathrm{eff}} = \alpha + \rho \frac{Q_L}{T} \left(\frac{\partial M}{\partial P} \right)_T \tag{14}$$

Advection of composition, temperature, strain, and stress fields is carried out in a Lagrangian manner using the particle-in-cell method. Particles are advected at each time step in an explicit manner using a 1^{st} order in time and 4^{th} order in space Runge-Kutta scheme.

2.2. Model setup

The numerical model domain consists of 400 (horizontal) by 200 (vertical) uniformly distributed nodes, giving physical dimensions of 200 km by 100 km resulting in a grid spacing of 500 m (Fig. 2A). The top of the model is a free surface that allows for accurate modelling topographic evolution (Duretz et al., 2016a). The geological model consists of a rectangular 30 km thick crust that is subdivided into two homogeneous components: a 2.5 km sedimentary cover on top of a 27.5 km granitic crust. The 2.5 km thick sedimentary cover is consistent with the thickness of the Paleoproterozoic sedimentary rocks present before reaching peak-metamorphic conditions of the Trans-Hudson Orogen (ca. 1.84 Ga; see Yeo and Delaney, 2007, in detail). A circular sedimentary inclusion (weak seed) with a diameter of 2 km was placed at a depth of 8.5 km and at x

= -10 km to initiate the deformation process. The rheological laws used in the experiments and the thermal parameters are presented in Table 1.

The boundary conditions applied to the model consist of an inflow (lateral boundaries of the model domain) and outflow (bottom) of material with a constant normal velocity. Since the size of the model box and applied shortening velocity will remain constant throughout the simulation, the corresponding average strain rate (i.e., $\dot{\varepsilon}_{\mathrm{BG}}$) applied at the boundaries is also constant. Material inflow is compensated by imposing a normal outflow at the bottom boundary, thus satisfying the mass conservation in the model's domain. In addition to variable values of average strain rates ($\dot{\varepsilon}_{\mathrm{BG}} = 10^{-14}$ s^{-1} to 10^{-16} s^{-1}), the models were conducted over a wide range of Moho temperatures (T_{Moho} = 550°C to 850°C). These ranges allowed us to simulate deformation patterns observed in both modern (cold and strong) and ancient (hot and weak) lithospheres. The initial geotherm was computed using thermal parameters (presented in Table 1) and a fixed temperature boundary of 1330°C at the base of the lithosphere. The geotherm was obtained by solving the heat equation until steady state and by varying the thickness of the lithosphere until the desired Moho temperature was reached. This constrains the initial thickness of the lithosphere.

Fig. 2B shows yield strength envelopes and geotherms corresponding to three primary deformation modes. These modes were obtained by considering three combinations of thermal profile and strain rate (T_{Moho} and $\dot{\varepsilon}_{\mathrm{BG}}$ values from left to right in Fig. 2B: [750°C, 1.e-14 s^{-1}], [650°C, 5.e-15 s^{-1}] and [750°C, 5.e-16 s^{-1}]). The corresponding lithospheric mantle depths for those models are 96, 141 and 96 km, respectively (Fig. 2B).

3. Results

Two governing parameters were considered: shortening rates ($\dot{\varepsilon}_{\mathrm{BG}}$) and Moho temperature ($T_{\mathrm{Moho}}$), to run 20 numerical simulations (see Appendix A for a summary of all experiments).

A summary of the parametric study results is presented in Fig. 3A together with the key features for each principal deformation style (Fig. 3B). These deformation styles, that have been identified by analysing the deformation of the sedimentary layer and the upper portions of the crust are, (i) pop-downs and upper crustal thrusting, (ii) a transitional deformation style, and (iii) sedimentary cusping. The deformation evolution of each model end member ($HS \sim 40$, 80, and 100 km) are presented in Figs. 4, 5, and 6, according to their morphology, viscosity, and accumulated strain, respectively. To further characterise the deformation modes, the topography evolution over time (Fig. 7) and the P-T-t paths of specific marker points (Fig. 8) are monitored. The marker points have been initially positioned within the sedimentary layer affected by burial throughout shortening and record the temperature and pressure evolution. The topographic range from the parametric study (Fig. 9) is defined by the minimum and maximum topography values up to $HS = 100$ km. Additionally, the distribution of deformation modes seen in the parametric study (Appendix. A) will also be mentioned.

3.1. Pop-downs and upper crustal thrusting

The first deformation style occurred when the lithosphere was subjected to high average strain rates ($\dot{\varepsilon}_{BG} = 10^{-14}$ s^{-1}). It was characterised by the occurrence of pop-down structures and the development of thrusts in the upper portions of the crust. The evolution of this deformation mode is seen in Fig. 4. This deformation mode, in comparison with the rest of the parametric study, occurs at high average strain rates for all tested geotherms (Fig. 3A). At high geotherms (e.g., $T_{\mathrm{Moho}} = 850°\mathrm{C}$), the geometry of the pop-downs and the resultant accumulated strain profile marks a possible transitional deformation mode (i.e., Fig. 3B, centre).

At the early stages of deformation, the upper portions of the crust began to experience periodic buckling with a slight downward deflection at the Moho ($HS = 40$ km in Fig. 4A, top and centre). From the viscosity field, the periodic buckling corresponds to the crests and troughs in the high viscosity triangular blocks ($\eta^{\mathrm{eff}} \geq 10^{22}$ Pa·s in Fig. 4A, centre), and their geometries extend to 20 km depth. The initial deformation is accompanied by a periodic strain pattern at a wavelength of 50 km that connects the upper portions of the crust and each new synform (Fig. 4A, bottom). At the next stage of deformation (at $HS \sim 80$ km), the amplitudes of the sedimentary synforms increase up to 20 km, evolving them to pop-downs (Fig. 4B). It is consistent with the geometry seen in previous analogue modelling experiments (Cagnard et al., 2006a). The corresponding high-viscosity triangular regions ($\eta^{\mathrm{eff}} \geq 10^{22}$ Pa·s in Fig. 4B, centre) increase in size and extend to a depth of 40 km. The upward deflection of the 800 MPa pressure isobar at $x = +5$ km near the base of the right pop-down indicates that an increase in pressure occurs during the descent of the pop-down. Overall finite strain increases throughout the model and begins to form two notable patterns (seen in Fig. 4B, bottom). The first pattern is a limited, vertically oriented finite strain band within and around the buried sedimentary cover. The second pattern corresponds to a preferential accumulation of strain from the surface to the upper portions of the pop-down. At $HS \sim 100$ km, the pop-downs merged to form a common 'valley' type topography feature (Fig. 4C, top). Between the merged pop-downs at a depth of 20 km, the upper portions of the crust are compressed to form a pinched antiform and are accompanied by an increase in pressure. The viscosity field confirms this observation with a high-viscosity, triangular-type pop-down ($\eta^{\mathrm{eff}} \geq 10^{22}$ Pa·s in Fig. 4C, centre). The viscosity of the aforementioned antiform is observed to be equally high. Below the pop-down cluster, the layering of the crust indicates a 'neutral surface' that is bounded by the 700°C isotherm.

By monitoring the topography evolution of the model, several important stages are identified (Fig. 7A). First, the buckling of the upper part of the model initiates a series of crests and troughs at $HS = 20$ km. Second, strain localises at $x =$ -60 km and 0 km forming a series of crests and troughs. Third, the topographic amplitude reached at 5 km with troughs and crests reaching -3 km and +2 km, respectively. The troughs develop from the formation of pop-downs. The most crucial point is the merging of the pop-downs at $HS = 80$ km where the troughs extend laterally from 2 km to 25 km. A low topographic relief region from $HS = 80$ km to 100 km undergoes lateral shortening towards a singular point. The topographic range for this reference model is 9.66 km in Fig. 9 and is consistent with other models that have presented a similar deformation style (e.g., $\dot{\varepsilon}_{\mathrm{BG}} = 10^{-14}$ s^{-1}, $T_{\mathrm{Moho}} = 550°\mathrm{C}$).

Finally, the P-T conditions of the buried sedimentary layer are observed within the kyanite mineral stability field (Fig. 8, black line), indicating high-pressure, low-temperature conditions. The tracked marker point (blue star in Fig. 4) at t = 1.57 Ma (red square in Fig. 8) reaches P-T conditions of 886 MPa and 236°C at $HS \sim 100$ km.

3.2. Transitioning from pop-downs to sedimentary cusping

The second reference model presents the generation of sedimentary corridors that appear geometrically similar to the sagducted Archean greenstone keels in granite-greenstone terranes (Fig. 1A, red box). Fig. 5 shows plots of the model evolution at increasing levels of horizontal shortening with the following initial conditions: T_{Moho}= 650°C, $\dot{\varepsilon}_{\mathrm{BG}} = 5 \times 10^{-15}$ s^{-1}. This deformation style is observed at moderately high average strain rates ($\dot{\varepsilon}_{\mathrm{BG}} = 5 \times 10^{-15}$ s^{-1}) for all tested geotherms.

The deformation evolution for this reference model is akin to the previously described pop-down reference model (Fig. 4), according to the following features: (i) the periodic buckling and folding at the upper portions of the crust, which correspond to the high-viscosity triangular crustal features ($\eta^{\mathrm{eff}} \geq 10^{22}$ Pa·s in Fig. 5, top and centre rows), (ii) the build-up of the periodic finite strain patterns that connect each new synform, and (iii) the vertically oriented strain patterns within the buried sedimentary features. The notable difference is the geometry of the buried sedimentary units. They do not conform to the geometry of the pop-downs as the units maintained a lateral thickness of at least 10 km (seen as high-viscosity crustal features at $\eta^{\mathrm{eff}} \geq 10^{22}$ Pa·s). The vertically oriented finite strain pattern within the sedimentary corridor has a vertical depth of 20 km, followed by two shear zones that extend laterally from the sedimentary corridor (Fig. 5C, bottom, at $x = +35$ km).

Topography evolution for this reference model (Fig. 7B) is comparable to the pop-down reference model described earlier. Periodic buckling of the upper portions of the crust starts with a series of crests and troughs of equal topography (of +2 km and -2 km respectively) at $HS > 20$ km. The amplitude of the synforms increases with increasing horizontal shortening and is close to the amplitude found in pop-downs formation (Cagnard et al., 2006b, and Fig. 1A). The sedimentary layer is buried asymmetrically, causing one of the troughs to reach a peak negative topography of -3 km ($x = 70$ km, $HS = 40$ km in Fig. 7B). The negative topography located at the other troughs is maintained throughout the deformation process, starting from -1.5 km from $HS = 40$ km. This reference model of the transitional deformation style attained a topographic range of 7.18 km (Fig. 9). When compared to other models showing a similar deformation style, high topographic ranges are generated here (ca. 7 to ca. 9.5 km in Fig. 9).

The P-T path of the sedimentary corridor (computed from the red stars shown in Fig. 5 and dashed lines in Fig. 8) is similar to the pop-down models (solid line in Fig. 8). The P-T conditions at $HS = 100$ km for both models remain within the kyanite stability zone. At 50% horizontal shortening, the tracked marker reaches a P-T condition of 798 MPa and 216°C.

3.3. Sedimentary cusping

This last deformation style occurs from moderate to low average strain rates ($\dot{\varepsilon}_{\mathrm{BG}} \leq 10^{-15}$ s^{-1}). Fig. 6 shows the evolution for progressive amounts of horizontal shortening with the following initial conditions (T_{Moho}= 750°C, $\dot{\varepsilon}_{BG}$ = 5×10^{-16} s^{-1}).

Similar to the other deformation styles, the upper portions of the crust begin to exhibit periodic buckling after reaching a crustal thickness greater than 40 km (seen in Fig. 6A). An initial build-up of strain connects the upper portions of the crust, forming wavelength ripples of around 50 km that progressively evolve in the sedimentary synforms of large amplitudes. The limit for the sedimentary synforms' amplitude is determined by the extent of the brittle portions of the crust ($\eta^{\text{eff}} \geq 10^{23}$ Pa·s in Fig. 6B, top and centre). Slivers of high viscosity are present beneath the aforementioned synforms, which may help strain localisation. Strain is localised within the sedimentary layer at x = -50 km and +35 km (Fig. 6B) as the result of continuous deformation. Further horizontal shortening leads to three notable effects that differ from the transitional deformation style (seen in Fig. 6C): (i) the sedimentary synform is more than half the lateral thickness of the sedimentary corridor, (ii) the depths ($>$ 20 km) of these sediments attain higher temperatures and lower pressure conditions compared to the aforementioned deformation styles (e.g., P = 530 MPa, T = 426°C at HS = 100 km seen in Fig. 8, red triangle), and (iii) limited vertical downward deflections of the 700°C isotherm (Fig. 6C) are observed. The number of downward deflections seen in the sedimentary cusping mode is small compared to the other deformation styles. It is characterised by the occurrence of crustal convection below 35 km in response to partial melting (Fig. 6C).

The overall topography evolution is smoother (Fig. 7C) when compared to the two previously mentioned reference models and deformation styles. Between $HS = 0$ and 8 km, the topography shows a widespread periodic buildup of crests and troughs with a values of +1 and -1 km before converging to form smaller waveforms (x = -70 km to +60 km). The maximum topography values reach -1.65 km to +1.65 km, having a maximum range of 3.3 km. This topographic range persists after the upper portions of the crust start buckling (HS = 40 km).

The P-T path of the tracked marker (black star in Fig. 6) for the sedimentary cusping example is hotter than those of the other deformation styles. At higher amounts of shortening ($HS > 100$ km), the sedimentary layer reaches partial melting P-T conditions and fall in the sillimanite stability field.

4. Discussion

4.1. Do pop-downs form when weak lithospheres are shortened?

The generation of pop-downs and the thrusting of the upper portions of the crust (Fig. 4) occurred at high to moderate-high average strain rates ($\dot{\varepsilon}_{\mathrm{BG}} \geq 5 \times 10^{-15}$ s^{-1}). The highest average strain rate from the parametric study leading to this deformation style ($\dot{\varepsilon}_{\mathrm{BG}} \geq 10^{-14}$ s^{-1}) corresponds to an extreme case of continuous shortening. The two pop-downs merged to form a single thrusting zone after the lithosphere achieved sufficient shortening. At moderately high average strain rates ($\dot{\varepsilon}_{\mathrm{BG}} \geq 5 \times 10^{-15}$ s^{-1}), the deformation features for the second reference model in Fig. 5 are comparable to those of the pop-downs and could be treated as a transitional deformation style (Fig. 3B, centre). The differences between these two deformation modes are based on the geometry of the buried sedimentary feature and the lower topographic range between 7 and 8 km. The thrusting of the upper portions of the crust and the development of shear zones from pop-down tectonics is analogous to deformation in modern-style lithospheres. Such deformation features consist in asymmetric deformation, capable of developing upper-crustal nappes, and are bounded by shear zones (as in e.g., Jaquet et al., 2018).

The results of the proposed tectonic framework were compared with previous analogue experiments (Cagnard et al., 2006a; Gapais et al., 2014; Gapais, 2018, and Fig. 1A). The symmetrical pop-downs and their merging (Fig. 4B and C) correspond to the initial stages of a pop-down development (Cagnard et al., 2006a). These features are identical to the structures observed in compressional salt tectonics (e.g., Brun and Fort, 2004). The series of pop-downs in our model consists of brittle growth synclines (sedimentary layer) and ductile pinched upper crustal antiforms (granitic crust). These deformational features appeared to reflect a strong mechanical control of the ductile granitic crust (Cagnard et al., 2006a).

As the pop-downs merged, shear zone forms and thrusting start to dominate (Fig. 4C, bottom). Meanwhile, buckling of the upper portions of the crust generated accommodation space for sediment accumulation (i.e., a trough). The burial of pop-downs along these newly developed shear zones was facilitated by shear heating that nucleated and promoted long-term strain localisation (Duretz et al., 2014; Thielmann and Kaus, 2012).

The generation of pop-downs was only observed in models at high average strain rates ($\dot{\varepsilon}_{\mathrm{BG}} \geq 5 \times 10^{-15}$ s^{-1}) for all tested geotherms (Fig. 3A). Higher geotherms (i.e., 850°C Moho) cause the lithospheric mantle to be weaker than the crust, thus fulfilling the classification of a créme brûlée' lithosphere (Burov et al., 2006). An increase of 100°C at the Moho (from 750° to 850°C) decrease the strength of the lithosphere by a factor of 4. Pop-downs were generated despite of a significantly weaker lithospheric mantle (see Fig. 3A and Appendix. A). Additional tests are required with other parameters (such as crustal radiogenic heat production and rheology) to map out the sensitivity of the proposed deformation styles. Furthermore, similar three-dimensional (3D) experiments would be necessary to account for lateral flows perpendicular to the direction of shortening (e.g., Rey and Houseman, 2006).

4.2. Role of buried sedimentary cover units for fluid flow

The burial of the sedimentary layer achieved depths greater than 20 km after 100 km of horizontal shortening in all tested models and without the need for an inverse density crustal profile. The finite strain patterns obtained within these sedimentary units were either vertically oriented, extending laterally from the corridor (transitional deformation style in Fig. 5) or concentrated within the cusp (sedimentary cusping in Fig. 6). The deformation style of interest was the sedimentary corridors within the pop-downs as it constitutes the closest analogue to what we see in the Mesoarchean East Pilbara Craton. The model thus helps to infer its potential fluid pathway capabilities. However, the similarities between our model and the field analogue are limited to the geometry of the deformed sedimentary cover and its internal structures.

The formation of the dome-and-basin structure described in the Mesoarchean East Pilbara Craton has been explained by the Archean sagduction/diaprism tectonic model (Fig. 1A, red box). Diaprism has been advocated by Kranendonk et al. (2004) through a series of geological, metamorphic, and structural observations to counter propose a tectonic evolution using uniformitarian processes (e.g., Bickle et al., 1985; van Haaften and White, 1998, and references therein). Gravitational instability of the dense greenstone layers was tested via numerical methods and found to be in agreement with the vertical structural network from the granitic domes and the sagducted vertical greenstone sheets in the field (see Thébaud and Rey, 2013). This vertical structural network is comparable to the vertical finite strain pattern within the sedimentary corridors and provides insight into its internal structural development (seen at $HS = 50$ km in Fig. 5C). Additionally, the generation of these sedimentary corridors did not require an 'inverted' density profile as the burial process could have been caused by the compressive tectonic regime.

The finite strain patterns within these sedimentary features could be interpreted as potential deep-rooted permeability-enhanced channels. We can hypothesise that such a network could focus fluid circulations and foster fluid-rock interactions. There are two possibilities: either an Archean ocean placed on top of the greenstone belt (e.g., Thébaud and Rey, 2013) or metamorphic fluids generated from dehydration reactions occurring at the depth in blueschist metamorphic facies conditions ($P \approx 800$ MPa, $T \approx 220°$C in Fig. 8 red circle). Au-enriched fluids from previous fluid inclusion data from quartz veins require a higher temperature ($T = 250°$C–$400°$C in Thébaud et al., 2006) when compared to the maximum P-T conditions of the buried sediments. Thus, a more shortened state might be required to meet this temperature requirement ($HS \geq 120$ km). But regardless of the fluid source, the P-T conditions at the base of the sedimentary corridor and vertical structures may help fluid transfers, potentially creating a feedback between mineralisation and generation of permeability-enhanced fluid channels (Cox, 2005).

4.3. Sedimentary cusping: Shortening of the hot and weak lithospheres over protracted periods

The cusping of the sedimentary layer and upper portions of the crust occurred at the lower compressive strain rates ($\dot{\varepsilon}_{\mathrm{BG}} \leq 10^{-15}$ s^{-1}), favouring the generation of deep-rooted vertical structures (Fig. 6). The buckling and subsequent pinching of the upper portions of the crust which formed high-amplitude and narrow wavelength synclines (lateral extents < 5 km) are inter-layered with antiforms of the upper portions of the granitic crust. The high-viscosity triangular crustal features ($\eta^{\mathrm{eff}} \geq 10^{23}$ Pa·s) that corresponded to pop-downs in previous reference models were absent in this model.

The geometry of the sedimentary cusps can be compared to large and wide Precambrian accretionary terranes ($>$ 500 km), such as the 3.0 Ga East Dharwar Craton (India; e.g., Chardon et al., 2009), the Finnish Southern Svecofennides (Cagnard et al., 2007) and the Terre Adelie Craton in Antarctica (Gapais et al., 2008). Typically, such accretionary terranes would experience long-lived and repeated juvenile magmatism and *HT-LP* metamorphism, which is coeval with crustal shortening over protracted periods (Cagnard et al., 2006a; Chardon et al., 2008, 2009; Collins and Vernon, 1991; Dumond et al., 2007; Gapais et al., 2005, 2014). Since the horizontal extent of the reference model was not as wide as stated in literature (e.g., Chardon et al., 2008, 2009), an additional test had to be conducted with a larger horizontal model domain to compare deformation evolutions (from $x = 200$ km to 400 km) for the three reference models. To ensure the scalability of the proposed deformation style, similar average strain rates that generated identical deformation features were used for the sedimentary cover in the extended model domain.

A key feature of Precambrian accretionary terranes is the presence of uniform metamorphic facies across the terrane. Achieving such a distribution has been hypothesised to be driven by widespread and distributed erosion competing with crustal thickening (Cagnard et al., 2007; Gapais et al., 2008). Our model results show some vertical downward deflections in the isotherms (Fig. 6C). The extent of the vertical deflections of the P-T contours decreased at higher geotherms (e.g., Appendix. A at $\dot{\varepsilon}_{\mathrm{BG}} = 5 \times 10^{-16}$ s^{-1}, $T_{\mathrm{Moho}} = 850$°C). If we consider a 20 km distributed erosion to this model, the distribution of the P-T conditions on the surface will be uniform. The resultant P-T condition at $HS = 100$ km corresponds to high-grade greenschist facies seen in Fig. 6C. A higher shortening of the lithosphere ($HS \sim 140$ km) will be able to bury the sediments at higher metamorphic conditions (up to granulite facies seen in the reference model for the Hearne Craton, discussed later in Sec. 4.4). The topographic range was observed to be 3.3 km, and this value continued to decrease in models at lower strain rates ($\dot{\varepsilon}_{\mathrm{BG}} < 10^{-15}$ s^{-1} as seen in Fig. 9).

Geometrical and potential structural evolutions from our model (Fig. 6) can be compared with the Archean Indian Dharwar Craton (Fig. 1A in Chardon et al., 2008). At $HS \sim 100$ km (Fig. 6C), the wavelength of the sedimentary cusps reaches 25 km, which corresponds to half the dimension of major shear zones. An additional test was conducted on an extended model domain, generating periodic sedimentary cusp of a similar wavelength at $HS \sim 94$ km. The finite strain within each sedimentary cusp is concentrated at the interface between the sedimentary layer and upper portions of the crust (e.g., z = -20 km in Fig. 6C). If we assume a 20 km distributed erosional event in this model, then the distribution of the steeply dipping finite strain patterns (Fig. 6C, bottom) may correlate to the foliation traces recorded within the upper portions of the crust (e.g., Chardon et al., 2002, 2008). Based on the agreement of the model with the geometric and structural features of the field examples mentioned above, we may conclude that the sedimentary cusping deformation style can be representative of Precambrian accretionary terranes.

4.4. Application to the Hearne Craton, Western Canadian Shield

The western Canadian shield of North America was formed from the accretion of several crustal blocks composed of Archean nuclei and Paleoproterozoic terranes. The Trans-Hudson orogen (THO, 1.84–1.78 Ga, Hoffman, 1988; Alexandre et al., 2007; Corrigan et al., 2009) is a good example of a Paleoproterozoic orogen that corresponds to global terrane accretion and orogenesis leading to the formation of the supercontinent Columbia (Nuna, 1.92–1.76 Ga, Kranendonk and Kirkland, 2016). It corresponds to the collision between the Superior Province to the east and the Hearne Province to the west (Fig. 10A). The Hearne Craton is constituted by the Mudjatik Domain, which is composed primarily of Archean gneiss domes and the Paleoproterozoic meta-sedimentary gneisses of the Wollaston Domain. These domains were imbricated during the Trans-Hudson orogen within the Mudjatik-Wollaston transition zone (WMTZ). This zone is characterised by a highly strained zone presenting steeply dipping anastomosed shear zones that extend over several hundred kilometres along-strike deformation (Fig. 10B). This tectonic evolution has been sealed between 1.7 Ga and 1.6 Ga with the deposition of the Athabasca basin that rests unconformably over these two deeply eroded domains.

The presence of high- to ultra-high-grade unconformity-related uranium deposits at the WMTZ, such as those of the McArthur River and Cigar Lake mines, attests to the widespread fluid-rock interactions between the major fault systems of the basement and its sedimentary cover. The origin of the vertical structures within the WMTZ and the Hearne Craton was examined in the framework of this thermo-mechanical study. Recent fluid-thermal simulations (e.g., Li et al., 2016, 2018) suggest that the reactivation of these inherited structures have played an important role in the formation of this metallogenic province.

4.4.1. Structural, metamorphic, temporal, and topography constraints

The deformation at the WMTZ has been described as an over-thickened crust with major SE-dipping reflectors, reactivated faults, and a 2 to 4 km wide SE-dipping listric shear zone (Annesley and Madore, 1994; Annesley et al., 2003; Hajnal et al., 1997). This is reflected in aeromagnetic and electromagnetic composite images showing an abrupt change of tectonic structures westwards from the Wollaston Domain (Fig. 10B). From east to west, the sub-vertical lineations and kilometre-scale ductile zones in the Paleoproterozoic Wollaston domains change into the more symmetrical dome and basin setting seen in the Archean Mudjatik Domain (Card et al., 2006).

These structures has been formed by Paleoproterozoic orogenic events (e.g., Corrigan et al., 2009; Whitmeyer and Karlstrom, 2007) leading to the THO, generating and concentrating a network of mylonitic zones. Mylonite zones are characterised by their steeply dipping foliations that bear sub-vertical stretching lineations (Tran et al., 1999) and by the burial and partially melted Paleoproterozoic sediments (Annesley et al., 2005). The sillimanite-cordierite metamorphic mineral assemblage found in Paleoproterozoic meta-sediments indicates a peak metamorphic condition at 800 MPa and 700°C during the THO at 1.84 Ga (Annesley et al., 2005). Recent fieldwork near Wollaston Lake has shown that this peak metamorphic period subsequently reached 10 kbars (Jeanneret et al., 2016).

The time required for the sedimentary rocks to be buried and achieve those metamorphic conditions is unknown, but we can ascertain some brackets. According to geochronological data available, the depositional ages of the Wollaston supergroup (i.e., Paleoproterozoic meta-sediments) range between (i) the detrital zircon ages in the NE Athabasca Basin at 2.54–1.92 Ga (Annesley et al., 1999; Tran et al., 2003) and (ii) the Pb-U zircon ages in the SE Athabasca Basin at 2.075–1.86 Ga (Ansdell et al., 2000; Tran et al., 2008). From these data points, the time range for the sedimentary rocks to be buried and achieve peak metamorphic conditions during THO would conservatively 20 Ma to 420 Ma.

The last constraint is to determine the topographic range at the eastern extents of the Athabasca Basin and the Hearne Craton. Before the peak-metamorphic THO, the accretion of the Rae and Hearne cratons generated the Snowbird Tectonic Line and orogenic activity (ca. 1.92–1.89 Ga Berman et al., 2007; Mahan et al., 2006, 2003, Fig. 10A). Previous observations near the boundary and at the northern extent of the Athabasca Basin has shown varying degrees of peak P-T conditions. These metamorphic peaks include the granulite facies rocks at the boundary of the tectonic terrane (Orlandini et al., 2018), higher pressure values at the western flank of the Snowbird Tectonic Line ($P > 900$ MPa, $T > 750$°C in Mahan et al., 2006), and low amphibolite facies conditions at the eastern flank ($P < 500$ MPa, $T \approx 600$–650°C Mahan et al., 2003). It has been suggested that these lower pressure rocks were a consequence of a localised thrusting event after peak-metamorphic THO from 1.84–1.78 Ga (Mahan et al., 2003). This highlighted a subsequent heterogeneous distribution of strain during accretion and localised tectonics that further complicate the distributed exhumation processes. At the SE extent of the WMTZ towards the Needle Falls shear zone (Fig. 10A), tectonic activity was seen to be equally active at the 1.89–1.87 Ga Lynn Lake and La Ronge arcs followed by the 1.865–1.85 Ga construction of the large magmatic arc (Corrigan et al., 2009). It has been suggested that these these accretion events occurred before the collision with the Hearne Craton margin (Corrigan et al., 2005). Although both flanks of the WMTZ were tectonically active ca. 1.84 Ga, associating the topographic range to P-T observations would be challenging to reconcile, especially when secondary tectonic forces are potentially in play (i.e., out of planar forces that require 3D modelling). A further complication was posed by unknown strain rates associated with the burial of these rocks at depth. Our modelling results suggest that the sediments capable of reaching the required P-T targets are associated with low ranges of topography and average strain rates. Therefore, we decided to constrain our modelling results with the first three parameters (i.e., structures, P-T conditions, and duration of convergence).

4.4.2. Determining the reference model for the WMTZ in the Hearne Craton

With sufficient horizontal shortening, the sedimentary layer can be buried at depths greater than 20 km, regardless of the magnitude of the average strain rate and geotherm (Fig. 3A and Appendix. A). The available geological and metamorphic data of the WMTZ-Hearne Craton allow us to determine a suitable reference model.

The P-T conditions for the sedimentary layer were compared to the P-T targets as the first constraint ($P_{\mathrm{Target}} \geq 8$ kbar, $T_{\mathrm{Target}} \geq 700°\mathrm{C}$). The models that agree with this P-T constraint had average strain rates of $\dot{\varepsilon}_{\mathrm{BG}} < 10^{-15}$ s^{-1}. The application of this constraint reduces the number of models within our parametric study to the models that featured the sedimentary cusping deformation style. The second constraint is the requirement of the presence of sub-vertical to vertical strain patterns seen in accumulated strain fields (Figs. 4, 5, 6 and Appendix A). Strain localisation within the upper portions of the crust has led to the burial of sediments. If these buried sediments were able to reach the P-T targets, the model can be considered as a potential reference model. The sedimentary cusping deformation style remained viable. The sediments in the sedimentary cusping models reach the P-T targets with sufficient horizontal shortening ($HS \sim 139$ km for Fig. 10D). The suggested reference model (Fig. 10D) remains viable at much higher HS conditions.

The last constraint required at least 20–420 Ma of convergence given by the upper and lower boundary ages of the Wollaston Supergroup. The remaining models with average strain rates of $\dot{\varepsilon}_{\mathrm{BG}} = 5 \times 10^{-16}$ s^{-1} and 10^{-16} s^{-1} required at least 43 Ma and 130 Ma of convergence, respectively, for the sedimentary layer to achieve the P-T targets (Fig. 10C). Based on our suggested constraints, the sedimentary cusping reference model (Fig. 10D) meets the requirements for a reference model of the WMTZ with 43.6 Ma of convergence. This suggests that the vertical structures has been formed by a long, sustained compressive regime, resulting in highly shortened states.

Although we determined the reference model using the first three constraints (i.e., P-T, vertical structures and time of convergence), addressing the topographic range as a possible constraint remains a challenge. The tectonic lines at the eastern and western flanks (i.e., the Needle Falls Shear Zone and the Snowbird Tectonic Line in Fig. 10A) has acted as a boundary for our study of areas having active orogenic activity. Although the proposed model has a maximum topographic range of 3.3 km (Fig. 9), this value indicates that mountain building processes are viable but not at the same scale as modern orogenic platforms, such as the Himalayan orogen (> 8 km in St-Onge et al., 2006). Lower strain rates reduced the overall strength of the lithosphere and have the potential to affect the ability of the lithosphere to support a high topography. The maximum topographic range in our parametric study progressively decreases at lower strain rates (Fig. 9). This implies that the surrounding regions away from the WMTZ affected by the THO receive varying levels of strain rates, thus highlighting the complexity of this multi-phase orogenic sequence.

4.4.3. Sedimentary cusping: the means to generate deep-rooted vertical structures

Shortly after peak THO metamorphic conditions were reached (ca. 1.84 Ga), widespread distributed erosional event of 20 km of crustal material has been proposed to accommodate isothermal decompression and calc-alkaline intrusions between 1.82 and 1.81 Ga (Annesley et al., 2005; Jeanneret et al., 2016). The application for this widespread exhumation event provided a first-order approach to determine the survival of ancient structures. The amount of material and its mechanism for exhumation remain debatable but we can suggest a couple of possibilities. First, a distributed erosion event of 30 km in our proposed model will be required to reveal a uniform and high metamorphic facies distribution seen at the southern Mudjatik Domain towards the transition zone (e.g., Lewry and Sibbald, 1980; Cagnard et al., 2011). Second, the effects of a reduction in tectonic activity can cause transpressive and strike-slip movements at a scale of hundreds of kilometres (Duclaux et al., 2007; Cagnard et al., 2006b) or the occurrence of localised tectonics (e.g., Mahan et al., 2003) capable of influencing the resulting exhumation processes. The combination of these possibilities may explain the exhumation process. However, accounting for this erosional behaviour and its effects on the redistribution of gravitational forces were out of the scope of this contribution.

Nevertheless, it was possible to consider this crustal removal event by comparing the structural features of the composite aeromagnetic and electromagnetic map (Fig. 10B) to the reference model ($HS \sim 138$ km in Fig. 10D). The general structural features within the WMTZ in the composite geophysics map and our proposed reference model (blue bi-directional arrows in Fig. 10B and D, top) show a region of a high concentration of sedimentary rocks. The layering of the upper portions of the crust seen from the morphological plot (Fig. 10D, top) has high amplitude fold-like features corresponding to the isoclinal folds at peak-metamorphic THO (e.g., Jeanneret et al., 2016), especially near Wollaston Lake at the NE portion of the WMTZ. The horizontal extent of this region is around 50 km (Fig. 10B) and is comparable to the horizontal extent of the structures found in the reference model (Fig. 10D). Due to the shortening process of the lithosphere in the model ($HS = 138$ km, marked by the two pins on the model), any deformational features that are laterally away from the pins are disregarded. Further horizontal shortening of a hot and mechanically weak model would result in a more homogeneous deformation.

Buckling of the upper crust and related synforms provided a good mechanism for the burial and diagenesis of sediments. Once the synforms reached critical amplitude (~ 15 km), synforms were pinched in response to strain localisation. Consequently, strain accumulated within the sediments. The additional horizontal shortening helped the suturing of these vertical strain zones to generate zones of deformed rocks (Fig. 10C, bottom). The amount of sediments reaching partial melting conditions can be approximated by the amplitude of the sedimentary cusp. Metamorphism and partial melting of the sedimentary layer may occur throughout the burial process, providing possible sources for hydrothermal fluids. This burial and deformation processes correlates to the mechanisms described and illustrated in Gapais et al. (2014) and Gapais (2018). When the sedimentary cusp reaches partial melting conditions, the lower portions of the buried sedimentary layer can detach and metasomatise at the lower portions of the crust. Furthermore, the verticality of the structures and sedimentary cusps is in agreement to deposit-scale cross-section drawings of McArthur and Southwest deposits (see Alexandre et al., 2007).

Despite structural and geometrical similarities with the field examples, caution must be taken regarding the interpretation of a lithosphere-scale thermomechanical model for two main reasons. One, it is unclear how deep these deep-rooted vertical structures within the crust extend at depth. Previous geophysical surveys close to the study area have shown these structures at depths greater than 25 km (line S1A and profile L in Hajnal et al. (2005) and Jones et al. (2005), respectively). However, both surveys were taken 300 km south from the Athabasca Basin. Therefore, the published results may not be representative for the study area. A follow up high resolution seismic imaging on the upper portions of the crust will be required to determine the extent of these vertical structures. Two, the ratio of the ductile to brittle portions of the crust exceeds the limitations of the lithosphere. As noted at the beginning of the discussion, 2D numerical modelling does not account for crustal flow in three dimensions, which is likely to be important during the shortening of hot and weak lithospheres (e.g., Duclaux et al., 2007; Chardon et al., 2008; Rey et al., 2010). However, we can speculate how a reorganisation of gravitational forces from an over-thickened crust is capable of triggering the transition from ca. 1.84 Ga peak-metamorphic THO, M1-D1, in Jeanneret et al. (2017) to an isothermal decompression, M2-D2, at 1.82–1.775 Ga (Annesley et al., 2005). This transition to a decompression regime has been interpreted as a sinistral transpressional force which leads to a significant decrease in pressure by 200 to 400 MPa (Jeanneret et al., 2016). Our proposed 2D reference model (Fig. 10D) can maintain its current lithospheric configuration while under sustained tectonic force. If this tectonic force subsides, the ductile portions of the crust will flow laterally perpendicular to the direction of shortening (i.e., out-of-plane motion) as a consequence of the balance of gravitational forces (Rey et al., 2010). The geotherm of the lithosphere in the reference model and the abundance of partial melting processes at the lower portions of the crust facilitate this perpendicular flow to the convergence direction. This may explain the occurrence of the sinistral transpressional event that marked M2-D2.

Partial melting has been included in the modelling process and led to crustal convection, which was particularly well-developed in the sedimentary cusping model (Fig. 6). Such effects are likely exaggerated because additional processes, such as melt extraction (requiring a two-phase flow formulation), have not been considered.

4.4.4. Potential implications to macro-scale fluid transport

The regional tectonic activity quietened after the last major deformation phase of the THO (i.e., the docking of the Superior Craton at ca. 1.8 Ga in Corrigan et al., 2009). The next major tectonic event involved a large scale exhumation of 20 km of crust (e.g., Annesley et al., 2005; Hajnal et al., 2005) and an uplift of the basement, followed by the deposition of the Athabasca Basin (∼ 1.7–1.75 Ga in Whitmeyer and Karlstrom, 2007). The first mineralisation event occurred 120 Ma after the deposition of the Athabasca Basin via the reactivation of the dormant underlying shear zones, triggering the mineralisation of uranium (e.g., Kyser et al., 2000; Mercadier et al., 2010; Martz et al., 2019). The presence of a sedimentary cusp and interconnecting structures would likely facilitate deep crustal hydrothermal fluid transport and circulation up to the surface (Fig. 10C, bottom), as suggested by Chi et al. (2018). This highlights the importance of the aforementioned structural architecture that is capable of predetermining future regions for uranium mineralisation. Predicting the loci for fluid convection cells around these ancient structures is now possible. Furthermore, the sedimentary cusping deformation model can also be used as a tectonic template for future thermal-fluid convection simulations.

5. Conclusions

The type of deformation zone generated from compressing lithospheres has often been assumed to be controlled by the thermal state of the lithosphere. It has also been suggested that ancient deformation zones such as those observed in Precambrian accretionary orogens underwent much longer periods of deformation (> 60 Ma) than in modern orogens, implying low average strain rates. Our 2D thermo-mechanical models investigate the role of shortening rates and geotherms (i.e., a wide range of lithospheric strength profiles). Our results highlight two main deformation styles controlled by the intensity of applied strain rates and allow to explain deformation styles found in natural examples (shear zones at the Indian Dharwar Craton and sedimentary corridors at the Mesoarchean East Pilbara Craton). Furthermore, the formation of vertical structures at the Wollaston-Mudjatik Transition Zone (Hearne Craton) can be explained by the sedimentary cusping deformation style. A proposed reference model for the Wollaston-Mudjatik Transition Zone was determined and fits with available geological, structural and metamorphic data. Predicting fluid flow patterns and mineralisation potential is now, therefore, possible by using formed vertical structures as a tectonic input for future thermal-fluid convection simulations.

Acknowledgments

This work represents the first portion of the first author's PhD thesis and is supported financially by Orano Canada Inc. The authors would like to thank Philippe Agard for smooth handling of the manuscript. Special thanks to Patrice Rey and Kevin Mahan for their comments and suggestions that significantly improved the quality of the manuscript. The 2D thermo-mechanical numerical code used for this work, MDoodz, can be made available on request by contacting either Philippe Yamato or Thibault Duretz. Special thanks to Philip Poh for proofreading the manuscript.

Alexandre, P., Kyser, K., Thomas, D., Polito, P., Marlat, J., 2007. Geochronology of unconformity-related uranium deposits in the Athabasca basin, Saskatchewan, Canada and their integration in the evolution of the basin. Mineralium Deposita 44, 41. doi:`10.1007/s00126-007-0153-3`.

Annesley, I., Madore, C., 1994. A geological study of the Wollaston-Mudjatik domain boundary in the Wollaston Lake area, Hearne Province, Saskatchewan. Saskatchewan Research Council. Technical Report. Publication R-1230-6-C-94.

Annesley, I.R., Madore, C., Hajnal, Z., 2003. Wollaston-Mudjatik transition zone : its characteristics and influence on the genesis of unconformity-type uranium deposits, in: International conference uranium geochemistry, pp. 55–58.

Annesley, I.R., Madore, C., Krogh, T.E., Kwok, Y., Kamo, S., 1999. New U–Pb zircon and monazite geochronological results for Archean and Paleoproterozoic basement to the southeastern part of the Athabasca Basin, Saskatchewan. Summary of investigations 2, 99–4.

Annesley, I.R., Madore, C., Portella, P., 2005. Geology and thermotectonic evolution of the western margin of the Trans-Hudson Orogen: evidence from the eastern sub-Athabasca basement, Saskatchewan. Canadian Journal of Earth Sciences 42, 573–597. doi:`10.1139/e05-034`.

Ansdell, K., MacNeill, A., Delaney, G., Hamilton, M., 2000. Rifting and development of the Hearne craton passive margin: age constraint from the Cook Lake area, Wollaston Domain, Trans-Hudson Orogen, Saskatchewan, in: GeoCanada 2000 Conference, Extended abstract, p. 777.

Artemieva, I.M., Mooney, W.D., 2001. Thermal thickness and evolution of Precambrian lithosphere: A global study. Journal of Geophysical Research: Solid Earth 106, 16387–16414. doi:`10.1029/2000jb900439`.

Berman, R., Davis, W., Pehrsson, S., 2007. Collisional Snowbird tectonic zone resurrected: Growth of Laurentia during the 1.9 Ga accretionary phase of the Hudsonian orogeny. Geology 35, 911–914. doi:`10.1130/G23771A.1`.

Bickle, M., Morant, P., Bettenay, L., Boulter, C., Blake, T., Groves, D., 1985. Archaean tectonics of the Shaw Batholith, Pilbara Block, Western Australia: structural and metamorphic tests of the batholith concept. Evolution of Archean Supracrustal Sequences 28, 325–341.

Bouhallier, H., Chardon, D., Choukroune, P., 1995. Strain patterns in Archaean dome-and-basin structures: The Dharwar craton (Karnataka, South India). Earth and Planetary Science Letters 135, 57–75. doi:`10.1016/0012-821X(95)00144-2`.

Brun, J.P., 2001. Deformation of the continental lithosphere: Insights from brittle-ductile models. Geological Society, London, Special Publications 200, 355–370. doi:10.1144/gsl.sp.2001.200.01.20.

Brun, J.P., Fort, X., 2004. Compressional salt tectonics (Angolan margin). Tectonophysics 382, 129 – 150. doi:10.1016/j.tecto.2003.11.014.

Burg, J.P., Gerya, T., 2005. The role of viscous heating in Barrovian metamorphism of collisional orogens: thermomechanical models and application to the Lepontine Dome in the Central Alps. Journal of Metamorphic Geology 23, 75–95. doi:10.1111/j.1525-1314.2005.00563.x.

Burov, E., Watts, A., et al., 2006. The long-term strength of continental lithosphere:" jelly sandwich" or" crème brûlée"? GSA today 16, 4.

Burov, E., Yamato, P., 2008. Continental plate collision, P–T–t–z conditions and unstable vs. stable plate dynamics: Insights from thermo-mechanical modelling. Lithos 103, 178 – 204. doi:10.1016/j.lithos.2007.09.014.

Burov, E.B., 2011. Rheology and strength of the lithosphere. Marine and Petroleum Geology 28, 1402 – 1443. doi:10.1016/j.marpetgeo.2011.05.008.

Cagnard, F., Barbey, P., Gapais, D., 2011. Transition between "Archaean-type" and "modern-type" tectonics: Insights from the Finnish Lapland Granulite Belt. Precambrian Research 187, 127–142. doi:10.1016/j.precamres.2011.02.007.

Cagnard, F., Brun, J.P., Gapais, D., 2006a. Modes of thickening of analogue weak lithospheres. Tectonophysics 421, 145–160. doi:10.1016/j.tecto.2006.04.016.

Cagnard, F., Durrieu, N., Gapais, D., Brun, J.P., Ehlers, C., 2006b. Crustal thickening and lateral flow during compression of hot lithospheres, with particular reference to Precambrian times. Terra Nova 18, 72–78. doi:10.1111/j.1365-3121.2005.00665.x.

Cagnard, F., Gapais, D., Barbey, P., 2007. Collision tectonics involving juvenile crust: The example of the southern Finnish Svecofennides. Precambrian Research 154, 125–141. doi:`10.1016/j.precamres.2006.12.011`.

Card, C.D., Harper, C.T., Barsi, N., Lesperance, J., Smith, J.S., 2006. Investigation of the Wollaston-Mudjatik Transition, Charcoal Lake and Cochrane River. Summary of Investigations 2, 1–16.

Cawood, P.A., Kroner, A., Pisarevsky, S., 2006. Precambrian plate tectonics: criteria and evidence. GSA today 16, 4.

Chardon, D., Gapais, D., Cagnard, F., 2009. Flow of ultra-hot orogens: A view from the Precambrian, clues for the Phanerozoic. Tectonophysics 477, 105 – 118. doi:`10.1016/j.tecto.2009.03.008`. hot orogens.

Chardon, D., Jayananda, M., Chetty, T.R.K., Peucat, J.J., 2008. Precambrian continental strain and shear zone patterns: South Indian case. Journal of Geophysical Research: Solid Earth 113. doi:`10.1029/2007jb005299`.

Chardon, D., Peucat, J.J., Jayananda, M., Choukroune, P., Fanning, C.M., 2002. Archean granite-greenstone tectonics at Kolar (South India): Interplay of diapirism and bulk in homogeneous contraction during juvenile magmatic accretion. Tectonics 21, 7–1–7–17. doi:`10.1029/2001tc901032`.

Chi, G., Li, Z., Chu, H., Bethune, K.M., Quirt, D.H., Ledru, P., Normand, C., Card, C., Bosman, S., Davis, W.J., et al., 2018. A shallow-burial mineralization model for the unconformity-related uranium deposits in the Athabasca Basin. Economic Geology 113, 1209–1217. doi:`10.5382/econgeo.2018.4588`.

Chopra, P.N., Paterson, M.S., 1984. The role of water in the deformation of dunite. Journal of Geophysical Research: Solid Earth 89, 7861–7876. doi:`10.1029/jb089ib09p07861`.

Choukroune, P., Bouhallier, H., Arndt, N.T., 1995. Soft lithosphere during periods of Archaean crustal growth or crustal reworking. Geological Society, London, Special Publications 95, 67–86. doi:10.1144/gsl.sp.1995.095.01.05.

Collins, W.J., Vernon, R.H., 1991. Orogeny associated with anticlockwise P-T-t paths: Evidence from low-P, high-T metamorphic terranes in the Arunta inlier, central Australia. Geology 19, 835. doi:10.1130/0091-7613(1991)019<0835:OAWAPT>2.3.CO;2.

Condie, K.C., Benn, K., 2013. Archean Geodynamics: Similar to or Different from Modern Geodynamics?. American Geophysical Union (AGU). pp. 47–59. doi:10.1029/164GM05.

Corrigan, D., Hajnal, Z., Németh, B., Lucas, S.B., 2005. Tectonic framework of a Paleoproterozoic arc-continent to continent-continent collisional zone, Trans-Hudson Orogen, from geological and seismic reflection studies. Canadian Journal of Earth Sciences 42, 421–434. doi:10.1139/e05-025.

Corrigan, D., Pehrsson, S., Wodicka, N., de Kemp, E., 2009. The Palaeoproterozoic Trans-Hudson Orogen: a prototype of modern accretionary processes. Geological Society, London, Special Publications 327, 457–479. doi:10.1144/SP327.19.

Cox, S., 2005. Coupling between deformation, fluid pressures, and fluid flow in ore-producing hydrothermal systems at depth in the crust. Economic Geology; Bulletin of the Society of Economic Geologists 100, 39–75.

Duclaux, G., Rey, P., Guillot, S., Ménot, R.P., 2007. Orogen-parallel flow during continental convergence: Numerical experiments and archean field examples. Geology 35, 715–718. doi:10.1130/G23540A.1.

Dumond, G., Mahan, K.H., Williams, M.L., Karlstrom, K.E., 2007. Crustal segmentation, composite looping pressure-temperature paths, and magma-enhanced metamorphic field gradients: Upper Granite Gorge, Grand Canyon, USA. Geological Society of America Bulletin 119, 202–220. doi:10.1130/b25903.1.

Duprat-Oualid, S., Yamato, P., Pitra, P., 2013. Major role of shear heating in intracontinental inverted metamorphism: Inference from a thermo-kinematic parametric study. Tectonophysics 608, 812 – 831. doi:`10.1016/j.tecto.2013.07.037`.

Duprat-Oualid, S., Yamato, P., Schmalholz, S.M., 2015. A dimensional analysis to quantify the thermal budget around lithospheric-scale shear zones. Terra Nova 27, 163–168. doi:`10.1111/ter.12144`.

Duretz, T., May, D.A., Yamato, P., 2016a. A free surface capturing discretization for the staggered grid finite difference scheme. Geophysical Journal International 204, 1518–1530. doi:`10.1093/gji/ggv526`.

Duretz, T., Petri, B., Mohn, G., Schmalholz, S.M., Schenker, F.L., Müntener, O., 2016b. The importance of structural softening for the evolution and architecture of passive margins. Scientific Reports 6, 38704. doi:`10.1038/srep38704`.

Duretz, T., Schmalholz, S., Podladchikov, Y., 2015. Shear heating-induced strain localization across the scales. Philosophical Magazine 95, 3192–3207. doi:`10.1080/14786435.2015.1054327`.

Duretz, T., Schmalholz, S.M., Podladchikov, Y.Y., Yuen, D.A., 2014. Physics-controlled thickness of shear zones caused by viscous heating: Implications for crustal shear localization. Geophysical Research Letters 41, 4904–4911. doi:`10.1002/2014GL060438`.

François, C., Philippot, P., Rey, P., Rubatto, D., 2014. Burial and exhumation during Archean sagduction in the East Pilbara granite-greenstone terrane. Earth and Planetary Science Letters 396, 235–251. doi:`10.1016/j.epsl.2014.04.025`.

Gapais, D., 2018. Tectonics-mineralisation relationships within weak continental lithospheres: a new structural framework for Precambrian cratons. Bulletin de la Société Géologique de France 189, 14. doi:`10.1051/bsgf/2018014`.

Gapais, D., Cagnard, F., Gueydan, F., Barbey, P., Ballèvre, M., 2009. Mountain building and exhumation processes through time: inferences from nature and models. Terra Nova 21, 188–194. doi:`10.1111/j.1365-3121.2009.00873.x`.

Gapais, D., Jaguin, J., Cagnard, F., Boulvais, P., 2014. Pop-down tectonics, fluid channelling and ore deposits within ancient hot orogens. Tectonophysics 618, 102–106. doi:`10.1016/j.tecto.2014.01.027`.

Gapais, D., Pelletier, A., Ménot, R.P., Peucat, J.J., 2008. Paleoproterozoic tectonics in the Terre Adélie Craton (East Antarctica). Precambrian Research 162, 531–539. doi:`10.1016/j.precamres.2007.10.011`.

Gapais, D., Potrel, A., Machado, N., Hallot, E., 2005. Kinematics of long-lasting Paleoproterozoic transpression within the Thompson Nickel Belt, Manitoba, Canada. Tectonics 24, TC3002. doi:`10.1029/2004TC001700`.

Gerya, T., 2009. Introduction to Numerical Geodynamic Modelling. Cambridge University Press.

Gerya, T.V., Yuen, D.A., 2003. Rayleigh–taylor instabilities from hydration and melting propel ‘cold plumes’ at subduction zones. Earth and Planetary Science Letters 212, 47–62. doi:`10.1016/S0012-821X(03)00265-6`.

Gray, R., Pysklywec, R.N., 2010. Geodynamic models of archean continental collision and the formation of mantle lithosphere keels. Geophysical Research Letters 37. doi:`10.1029/2010GL043965`.

van Haaften, W., White, S., 1998. Evidence for multiphase deformation in the Archean basal Warrawoona Group in the Marble Bar area, East Pilbara, Western Australia. Precambrian Research 88, 53 – 66. doi:`10.1016/S0301-9268(97)00063-6`.

Hajnal, Z., Lewry, J., White, D., Ashton, K., Clowes, R., Stauffer, M., Gyorfi, I., Takacs, E., 2005. The Sask Craton and Hearne Province margin: seismic reflection studies in the western Trans-Hudson Orogen. Canadian Journal of Earth Sciences 42, 403–419. doi:`10.1139/e05-026`.

Hajnal, Z., Nemeth, B., Clowes, R.M., Ellis, R.M., Spence, G.D., Burianyk, M.J.A., Asudeh, I., White, D.J., Forsyth, D.A., 1997. Mantle involvement in lithospheric collision: Seismic evidence from the Trans-Hudson Orogen, western Canada. Geophysical Research Letters 24, 2079–2082. doi:`10.1029/97gl01958`.

Hansen, F., Carter, N., 1983. Semibrittle creep of dry and wet Westerly granite at 1000 MPa. The 24th US Symposium on Rock Mechanics (USRMS) .

Hirth, G., Kohlstedt, D., 2004. Rheology of the Upper Mantle and the Mantle Wedge: A View from the Experimentalists. American Geophysical Union (AGU). doi:`10.1029/138GM06`.

Hoffman, P.F., 1988. United Plates of America, The Birth of a Craton: Early Proterozoic Assembly and Growth of Laurentia. Annual Review of Earth and Planetary Sciences 16, 543–603. doi:`10.1146/annurev.ea.16.050188.002551`.

Holdaway, M.J., 1971. Stability of andalusite and the aluminum silicate phase diagram. American Journal of Science 271, 97–131. doi:`10.2475/ajs.271.2.97`.

Jackson, J.A., 2002. Strength of the continental lithosphere : Time to abandon the jelly sandwich? GSA Today 12, 4–10. doi:`10.1130/1052-5173(2002)012<0004:SOTCLT>2.0.CO;2`.

Jaquet, Y., Duretz, T., Grujic, D., Masson, H., Schmalholz, S.M., 2018. Formation of orogenic wedges and crustal shear zones by thermal softening, associated topographic evolution and application to natural orogens. Tectonophysics 746, 512 – 529. doi:`10.1016/j.tecto.2017.07.021`.

Jaupart, C., Mareschal, J., Watts, A., 2007. Heat flow and thermal structure of the lithosphere. Treatise on Geophysics 6, 217–252.

Jeanneret, P., Goncalves, P., Durand, C., Poujol, M., Trap, P., Marquer, D., Quirt, D., Ledru, P., 2017. Geochronological constraints on the Trans-

Hudsonian tectono-metamorphic evolution of the pre-Athabasca basement within the Wollaston-Mudjatik Transition Zone, Saskatchewan. Precambrian Research 301, 152–178. doi:`10.1016/j.precamres.2017.07.019`.

Jeanneret, P., Goncalves, P., Durand, C., Trap, P., Marquer, D., Quirt, D., Ledru, P., Rivers, T., 2016. Tectono-metamorphic evolution of the pre-Athabasca basement within the Wollaston–Mudjatik Transition Zone, Saskatchewan. Canadian Journal of Earth Sciences 53, 231–259. doi:`10.1139/cjes-2015-0136`.

Jones, A.G., Ledo, J., Ferguson, I.J., 2005. Electromagnetic images of the trans-hudson orogen: the north american central plains anomaly revealed. Canadian Journal of Earth Sciences 42, 457–478. doi:`10.1139/e05-018`.

Kelemen, P.B., Hirth, G., 2007. A periodic shear-heating mechanism for intermediate-depth earthquakes in the mantle. Nature 446, 787–790. doi:`10.1038/nature05717`.

Kranendonk, M.J.V., Collins, W., Hickman, A., Pawley, M.J., 2004. Critical tests of vertical vs. horizontal tectonic models for the Archaean East Pilbara Granite-Greenstone Terrane, Pilbara Craton, Western Australia. Precambrian Research 131, 173 – 211. doi:`10.1016/j.precamres.2003.12.015`.

Kranendonk, M.J.V., Kirkland, C.L., 2016. Conditioned duality of the earth system: Geochemical tracing of the supercontinent cycle through earth history. Earth-Science Reviews 160, 171 – 187. doi:`10.1016/j.earscirev.2016.05.009`.

Kyser, K., Hiatt, E., Renac, C., Durocher, K., Holk, G., Deckart, K., 2000. Diagenetic fluids in Paleo-and Meso-Proterozoic sedimentary basins and their implications for long protracted fluid histories. Mineralogical Association of Canada Short Course 28, 225–262.

Lewry, J.F., Sibbald, T.I., 1980. Thermotectonic evolution of the Churchill province in Northern Saskatchewan. Tectonophysics 68, 45 – 82. doi:10.1016/0040-1951(80)90008-6.

Li, Z., Chi, G., Bethune, K., 2016. The effects of basement faults on thermal convection and implications for the formation of unconformity-related uranium deposits in the Athabasca Basin, Canada. Geofluids 16, 729–751.

Li, Z., Chi, G., Bethune, K.M., Eldursi, K., Thomas, D., Quirt, D., Ledru, P., 2018. Synchronous egress and ingress fluid flow related to compressional reactivation of basement faults: the Phoenix and Gryphon uranium deposits, southeastern Athabasca Basin, Saskatchewan, Canada. Mineralium Deposita 53, 277–292.

Liao, J., Gerya, T., 2017. Partitioning of crustal shortening during continental collision: 2-D thermomechanical modeling. Journal of Geophysical Research: Solid Earth 122, 592–606. doi:10.1002/2016jb013398.

Mahan, K.H., Williams, M.L., Baldwin, J.A., 2003. Contractional uplift of deep crustal rocks along the Legs Lake shear zone, western Churchill Province, Canadian Shield. Canadian Journal of Earth Sciences 40, 1085–1110. doi:10.1139/e03-039.

Mahan, K.H., Williams, M.L., Flowers, R.M., Jercinovic, M.J., Baldwin, J.A., Bowring, S.A., 2006. Geochronological constraints on the legs lake shear zone with implications for regional exhumation of lower continental crust, western Churchill Province, Canadian Shield. Contributions to Mineralogy and Petrology 152, 223–242. doi:10.1007/s00410-006-0106-3.

Martz, P., Mercadier, J., Cathelineau, M., Boiron, M.C., Quirt, D., Doney, A., Gerbeaud, O., Wally, E.D., Ledru, P., 2019. Formation of U-rich mineralizing fluids through basinal brine migration within basement-hosted shear zones: A large-scale study of the fluid chemistry around the unconformity-related Cigar Lake U deposit (Saskatchewan, Canada). Chemical Geology 508, 116 – 143. doi:10.1016/j.chemgeo.2018.05.042. advances in Fluid and Melt Inclusion Research.

McGuire, J.J., Beroza, G.C., 2012. A Rogue Earthquake Off Sumatra. Science 336, 1118–1119. doi:`10.1126/science.1223983`.

Mercadier, J., Richard, A., Boiron, M.C., Cathelineau, M., Cuney, M., 2010. Migration of brines in the basement rocks of the Athabasca Basin through microfracture networks (P-Patch U deposit, Canada). Lithos 115, 121 – 136. doi:`10.1016/j.lithos.2009.11.010`.

Orlandini, O.F., Mahan, K.H., Williams, M.J., Regan, S.P., Mueller, K.J., 2018. Evidence for deep crustal seismic rupture in a granulite-facies, intraplate, strike-slip shear zone, northern Saskatchewan, Canada. Bulletin 131, 403–425. doi:`10.1130/B31922.1`.

Pattison, D.R.M., 1992. Stability of Andalusite and Sillimanite and the Al_2SiO_5 triple point: Constraints from the Ballachulish Aureole, Scotland. The Journal of Geology 100, 423–446. doi:`10.1086/629596`.

Pfiffner, O.A., Ramsay, J.G., 1982. Constraints on geological strain rates: Arguments from finite strain states of naturally deformed rocks. Journal of Geophysical Research: Solid Earth 87, 311–321. doi:`10.1029/jb087ib01p00311`.

Poli, S., Schmidt, M.W., 2002. Petrology of subducted slabs. Annual Review of Earth and Planetary Sciences 30, 207–235. doi:`10.1146/annurev.earth.30.091201.140550`.

Ranalli, G., 1995. Rheology of the Earth. Springer Science & Business Media.

Ranalli, G., 1997. Rheology of the lithosphere in space and time. Geological Society, London, Special Publications 121, 19–37. doi:`10.1144/gsl.sp.1997.121.01.02`.

Rey, P.F., Coltice, N., 2008. Neoarchean lithospheric strengthening and the coupling of earth's geochemical reservoirs. Geology 36, 635–638. doi:`10.1130/G25031A.1`.

Rey, P.F., Houseman, G., 2006. Lithospheric scale gravitational flow: the impact of body forces on orogenic processes from Archaean to Phanerozoic. Geological Society, London, Special Publications 253, 153–167. doi:`10.1144/gsl.sp.2006.253.01.08`.

Rey, P.F., Teyssier, C., Whitney, D.L., 2010. Limit of channel flow in orogenic plateaux. Lithosphere 2, 328–332.

Schmidt, M.W., Poli, S., 1998. Experimentally based water budgets for dehydrating slabs and consequences for arc magma generation. Earth and Planetary Science Letters 163, 361 – 379. doi:`10.1016/S0012-821X(98)00142-3`.

St-Onge, M.R., Searle, M.P., Wodicka, N., 2006. Trans-Hudson orogen of North America and Himalaya-Karakoram-Tibetan orogen of Asia: Structural and thermal characteristics of the lower and upper plates. Tectonics 25, 1–22. doi:`10.1029/2005TC001907`.

Thébaud, N., Philippot, P., Rey, P., Brugger, J., Van Kranendonk, M., Grassineau, N., 2008. Protracted fluid–rock interaction in the Mesoarchaean and implication for gold mineralization: Example from the Warrawoona syncline (Pilbara, Western Australia). Earth and Planetary Science Letters 272, 639–655. doi:`10.1016/j.epsl.2008.05.030`.

Thébaud, N., Philippot, P., Rey, P., Cauzid, J., 2006. Composition and origin of fluids associated with lode gold deposits in a Mesoarchean greenstone belt (Warrawoona Syncline, Pilbara Craton, Western Australia) using synchrotron radiation X-ray fluorescence. Contributions to Mineralogy and Petrology 152, 485.

Thébaud, N., Rey, P., 2013. Archean gravity-driven tectonics on hot and flooded continents: Controls on long-lived mineralised hydrothermal systems away from continental margins. Precambrian Research 229, 93 – 104. doi:`10.1016/j.precamres.2012.03.001`.

Thielmann, M., Kaus, B.J., 2012. Shear heating induced lithospheric-scale localization: Does it result in subduction? Earth and Planetary Science Letters 359-360, 1 – 13. doi:`10.1016/j.epsl.2012.10.002`.

Toussaint, G., Burov, E., Avouac, J.P., 2004. Tectonic evolution of a continental collision zone: A thermomechanical numerical model. Tectonics 23, 1–24. doi:`10.1029/2003tc001604`.

Tran, H.T., Ansdell, K., Bethune, K., Watters, B., Ashton, K., 2003. Nd isotope and geochemical constraints on the depositional setting of Paleoproterozoic metasedimentary rocks along the margin of the Archean Hearne craton, Saskatchewan, Canada. Precambrian Research 123, 1 – 28. doi:`10.1016/S0301-9268(03)00012-3`.

Tran, H.T., Ansdell, K.M., Bethune, K.M., Ashton, K., Hamilton, M.A., 2008. Provenance and tectonic setting of Paleoproterozoic metasedimentary rocks along the eastern margin of Hearne craton: Constraints from SHRIMP geochronology, Wollaston group, Saskatchewan, Canada. Precambrian Research 167, 171 – 185. doi:`10.1016/j.precamres.2008.08.003`.

Tran, H.T., Yeo, G., Bethune, K., 1999. Geology of the McKenzie Falls area, Haultain River, Wollaston-Mudjatik domains boundary (NTS 74B-7 and -8). Technical Report. Saskatchewan Geological Survey. Saskatchewan.

Turcotte, D., Schubert, G., 2002. Geodynamics. Cambridge University Press.

Whitmeyer, S.J., Karlstrom, K.E., 2007. Tectonic model for the Proterozoic growth of North America. Geosphere 3, 220. doi:`10.1130/GES00055.1`.

Yamato, P., Duretz, T., Angiboust, S., 2019. Brittle/ductile deformation of eclogites: Insights from numerical models. Geochemistry, Geophysics, Geosystems doi:`10.1029/2019GC008249`.

Yeo, G.M., Delaney, G., 2007. The Wollaston supergroup, stratigraphy and metallogeny of a Paleoproterozoic Wilson cycle in the Trans-Hudson Orogen, Saskatchewan. Bulletin of the Geological Survey of Canada , 89–117.

Table and Figure captions

	Sedimentary Layer	**Crust**	**Lithospheric Mantle**	**Asthenosphere**
Rheological Properties				
Material	Dry Quartz	Dry Westerly Granite	Dry Olivine	Dry Olivine
n	2.4	3.3	3.0	3.0
A [Pa^{-n}.s^{-1}]	2.67×10^{-20}	3.16×10^{-26}	7.0×10^{-15}	7.0×10^{-15}
Q [J.mol^{-1}]	156.0×10^{3}	186.5×10^{3}	510.4×10^{3}	510.4×10^{3}
C_0 [Pa]	10.0×10^{6}	10.0×10^{6}	10.0×10^{6}	10.0×10^{6}
tan(ϕ)	0.6	0.6	0.6	0.6
ρ_0^{solid} [kg.m^{-3}]	2,800	2,800	3,300	3,300
References	1, 2	3	4	4
Crustal partial melting equations[5,6]				
$T_{solidus}$ [K]	973 - 70,400/(P + 354) + 77,800,000/(P + 354)^2 if $P < 1{,}600$ MPa and 935 + 0.0035P + 0.0000062P^2 if $P > 1{,}600$ MPa		1394 + 0.132899P - 0.000005014P^2 if $P < 10{,}000$ MPa and 2212 + 0.030819(P - 10,000) if $P > 10{,}000$ MPa	
$T_{liquidus}$ [K]	1423 + 0.105P	1423 + 0.105P	2073 + 0.114P	2073 + 0.114P
$\Delta\rho_0^{\text{molten}}$ [kg.m^{-3}]	250	250	250	250
$Q_L^{7,8}$ [J.kg^{-1}]	380,000	380,000	400,000	400,000
Thermal Properties				
^{9}k [W.K^{-1}.m^{-1}]	2.3	2.3	3.0	3.0×10^{5}
^{9}Cp [J.kg^{-1}.K^{-1}]	1,050	1,050	1,050	1,050
κ [m^2.s^{-1}]	7.82×10^{-7}	7.82×10^{-7}	8.66×10^{-7}	0.87
H_R^{b} [W.m^{-3}]	2.0×10^{-6}	2.0×10^{-6}	2.2×10^{-8}	1.0×10^{-10}
$^{10}\alpha$ [K^{-1}]	3.0×10^{-5}	3.0×10^{-5}	3.0×10^{-5}	3.0×10^{-5}
$^{10}\beta$ [Pa^{-1}]	1.0×10^{-11}	1.0×10^{-11}	1.0×10^{-11}	1.0×10^{-11}

Table 1: Rheological and thermal values used for the numerical model. Rheological laws are solved using axial compression formulas in Gerya (2009). References for rheology and partial melting are 1: Ranalli (1995), 2: Ranalli (1997), 3: Hansen and Carter (1983), 4: Chopra and Paterson (1984), 5: Schmidt and Poli (1998), 6: Poli and Schmidt (2002), 7: Turcotte and Schubert (2002), and 8: Gerya (2009). References for thermal properties are [9] Turcotte and Schubert (2002) and [10] Liao and Gerya (2017).

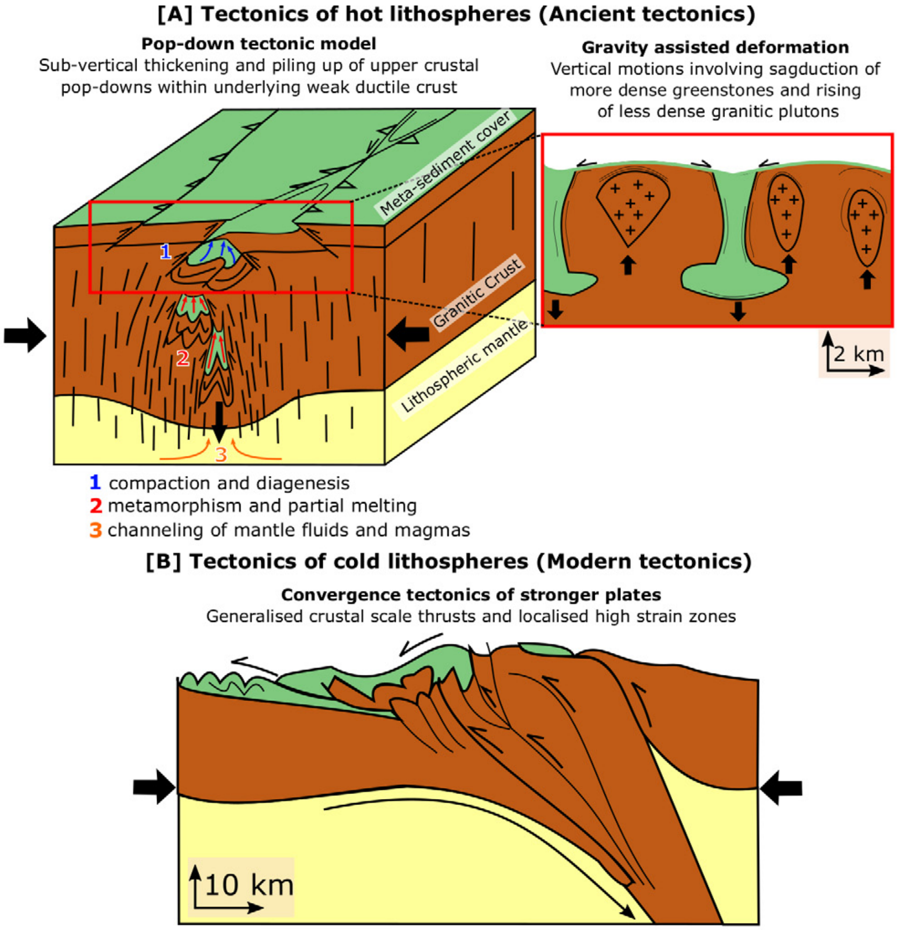

Figure 1: Schematic models illustrating general deformation patterns observed in convergent continental lithospheres. (A) The pop-down tectonic model underlying the progressive burial of crustal material is expected to be accompanied by fluid release and transfer during compaction, diagenesis, and eventual metamorphism and partial melting. Magma production and interactions with the lithospheric mantle may also contribute to fluid-rock interactions. Modified from Cagnard et al. (2006a), Gapais et al. (2014) and Gapais (2018). The red box on the left panel highlights the effects of body forces (i.e., gravity) to meta-sediment compaction and burial (seen in the right panel). The general pattern of gravity-driven deformation models for Archaean tectonics, which generally involve the rising of hot and partially melted crust (diapirism) and the sinking of dense greenstone belts (sagduction). Drawing from Choukroune et al. (1995) and Cagnard et al. (2007). (B) Classical shortening of a cold and strong lithospheric mantle that favours crustal-scale thrusts and shear zones, modified from Cagnard et al. (2011). Colours of the geological layers correspond to the numerical model in Fig. 2.

Figure 1: Schematic models illustrating general deformation patterns observed in convergent continental lithospheres. (A) The pop-down tectonic model underlying the progressive burial of crustal material is expected to be accompanied by fluid release and transfer during compaction, diagenesis, and eventual metamorphism and partial melting. Magma production and interactions with the lithospheric mantle may also contribute to fluid-rock interactions. Modified from Cagnard et al. (2006a), Gapais et al. (2014) and Gapais (2018). The red box on the left panel highlights the effects of body forces (i.e., gravity) to meta-sediment compaction and burial (seen in the right panel). The general pattern of gravity-driven deformation models for Archaean tectonics, which generally involve the rising of hot and partially melted crust (diapirism) and the sinking of dense greenstone belts (sagduction). Drawing from Choukroune

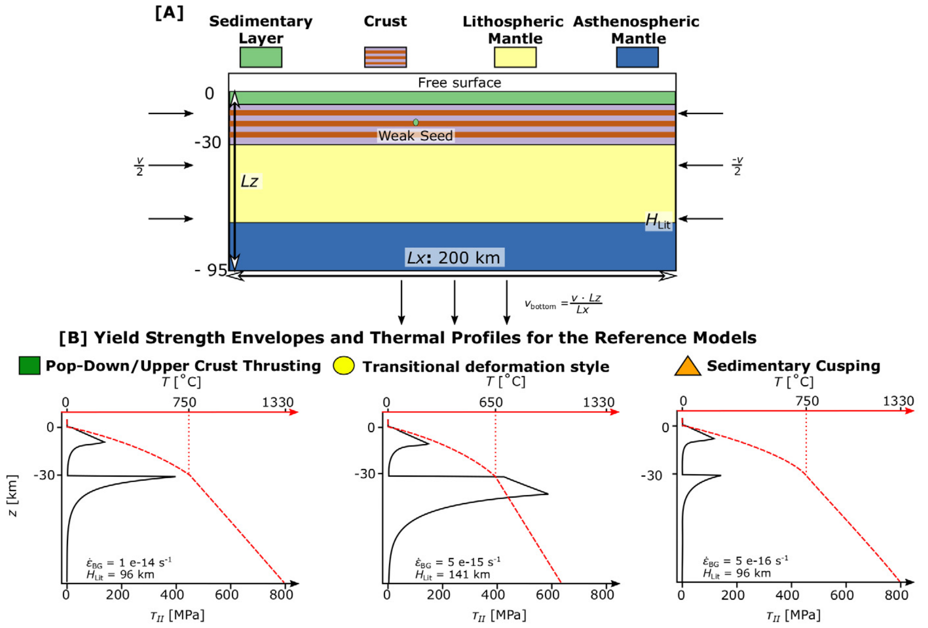

Figure 2: (A) Model domain setup and boundary conditions (see text for details). Colours indicate rock type that appear in morphology plots in subsequent figures. *V* represents the convergence velocities computed from $\dot{\varepsilon}_{\mathrm{BG}}$. (B) Temperature profiles (red) and initial lithospheric strength profiles (black) for tectonic end members. From right to left: Pop-downs/Upper crustal thrusting, transitional deformation style, Sedimentary cusping. Notice the changes in $\dot{\varepsilon}_{\mathrm{BG}}$ when constructing the lithospheric strength profiles.

Figure 2: (A) Model domain setup and boundary conditions (see text for details). Colours indicate rock type that appear in morphology plots in subsequent figures. V represents the convergence velocities computed from $\dot{\varepsilon}_{\mathrm{BG}}$. (B) Temperature profiles (red) and initial lithospheric strength profiles (black) for tectonic end members. From right to left: Pop-downs/Upper crustal thrusting, transitional deformation style, Sedimentary cusping. Notice the changes in $\dot{\varepsilon}_{\mathrm{BG}}$ when constructing the lithospheric strength profiles.

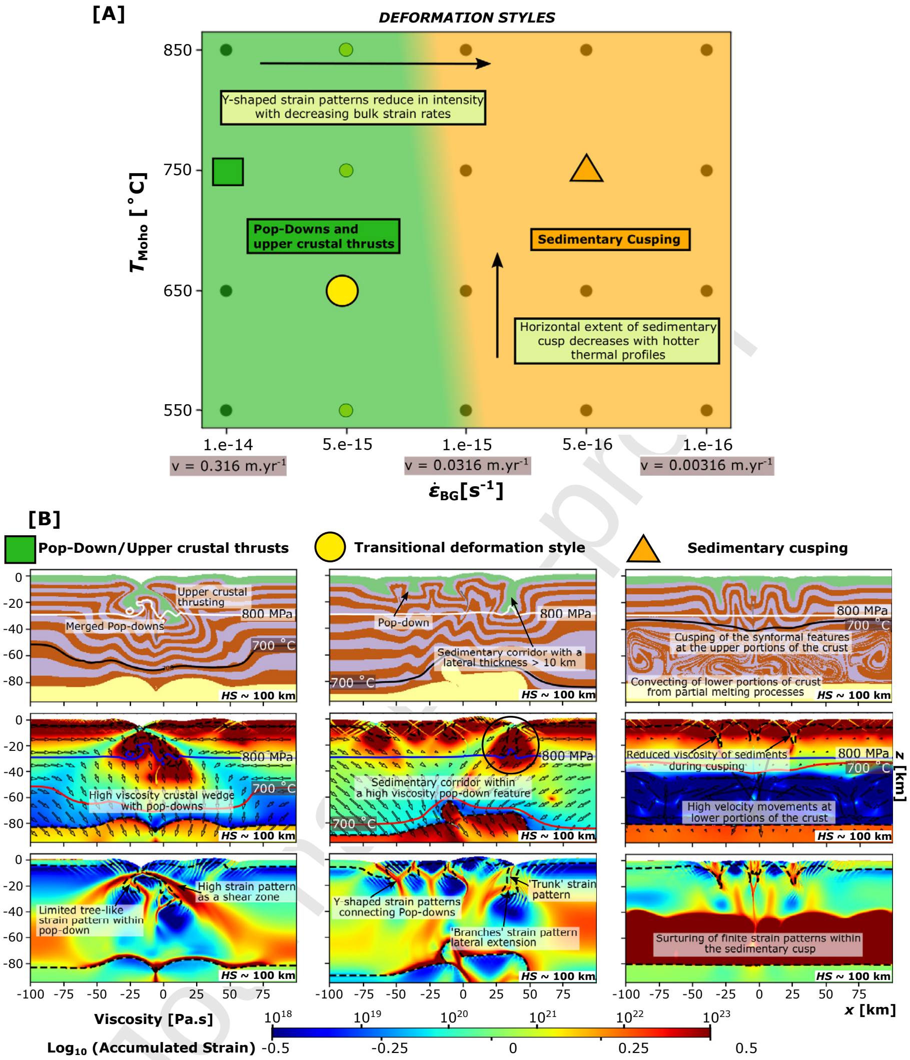

Figure 3: Key deformation styles found in the parametric study. (A) Summary of tectonic features with a range of average strain rates ($\dot{\varepsilon}_{\mathrm{BG}}$) and Moho temperatures (T_{Moho}). Black dots represent performed experiments. (B) Representative snapshots of the main deformation styles are highlighted (from left to right): Pop-Down and upper crustal thrusting, transitional deformation style, and sedimentary cusping. Figures show morphology (top), viscosity (centre) and accumulated strain (bottom). The 800 MPa isobar and 700°C isotherms are represented by the white and black lines in the morphology field and blue and red lines in the viscosity field.

Figure 3: Key deformation styles found in the parametric study. (A) Summary of tectonic features with a range of average strain rates ($\dot{\epsilon}_{\mathrm{BG}}$) and Moho temperatures (T_{Moho}). Black dots represent performed experiments. (B) Representative snapshots of the main deformation styles are highlighted (from left to right): Pop-Down and upper crustal thrusting, transitional deformation style, and sedimentary cusping. Figures show morphology (top), viscosity (centre) and accumulated strain (bottom). The 800 MPa isobar and 700°C isotherms are represented by the white and black lines in the morphology field and blue and red lines in the viscosity field.

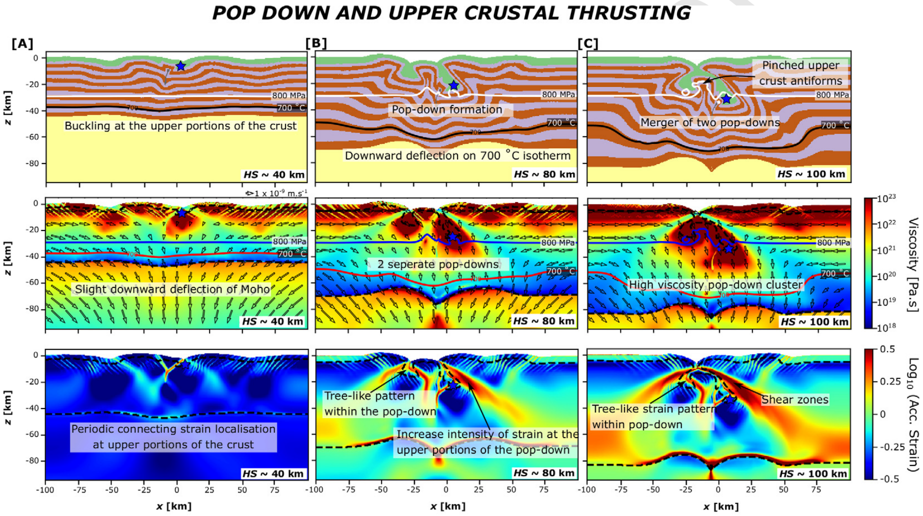

Figure 4: Pop-down and upper crustal thrusting end member evolution at high average strain rates ($\dot{\varepsilon}_{\mathrm{BG}}$ = 10^{-14} s^{-1}). Evolution over time (*HS* corresponds to horizontal shortening) of morphology (top row), viscosity (centre row), and accumulated strain fields (bottom row). The deformation evolution will be presented in a similar format in Figs. 5 and 6.

Figure 4: Pop-down and upper crustal thrusting end member evolution at high average strain rates ($\dot{\varepsilon}_{\mathrm{BG}} = 10^{-14}\ \mathrm{s}^{-1}$). Evolution over time (*HS* corresponds to horizontal shortening) of morphology (top row), viscosity (centre row), and accumulated strain fields (bottom row). The deformation evolution will be presented in a similar format in Figs. 5 and 6.

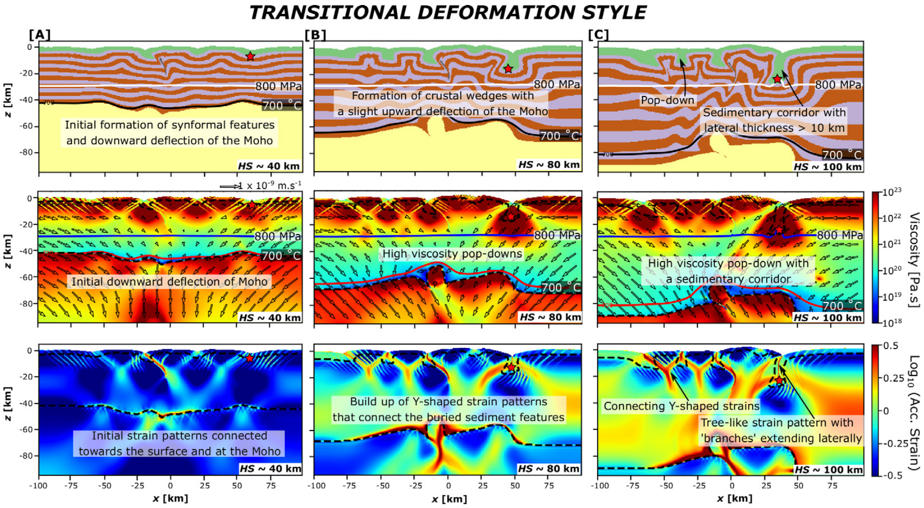

Figure 5: Evolution of the transitional deformation style at moderately high average strain rates ($\dot{\varepsilon}_{BG}$ = 5 x 10^{-15} s^{-1}).

Figure 5: Evolution of the transitional deformation style at moderately high average strain rates ($\dot{\varepsilon}_{\mathrm{BG}} = 5 \times 10^{-15}\ \mathrm{s}^{-1}$).

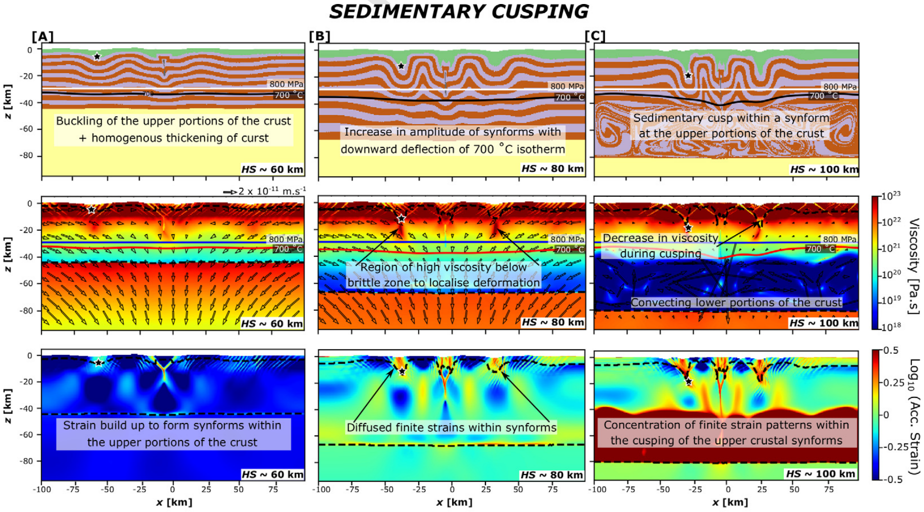

Figure 6: Sedimentary cusping end member evolution at moderately low average strain rates ($\dot{\varepsilon}_{BG}$ = 5 x 10^{-16} s^{-1}).

Figure 6: Sedimentary cusping end member evolution at moderately low average strain rates ($\dot{\varepsilon}_{\mathrm{BG}} = 5 \times 10^{-16}\ \mathrm{s}^{-1}$).

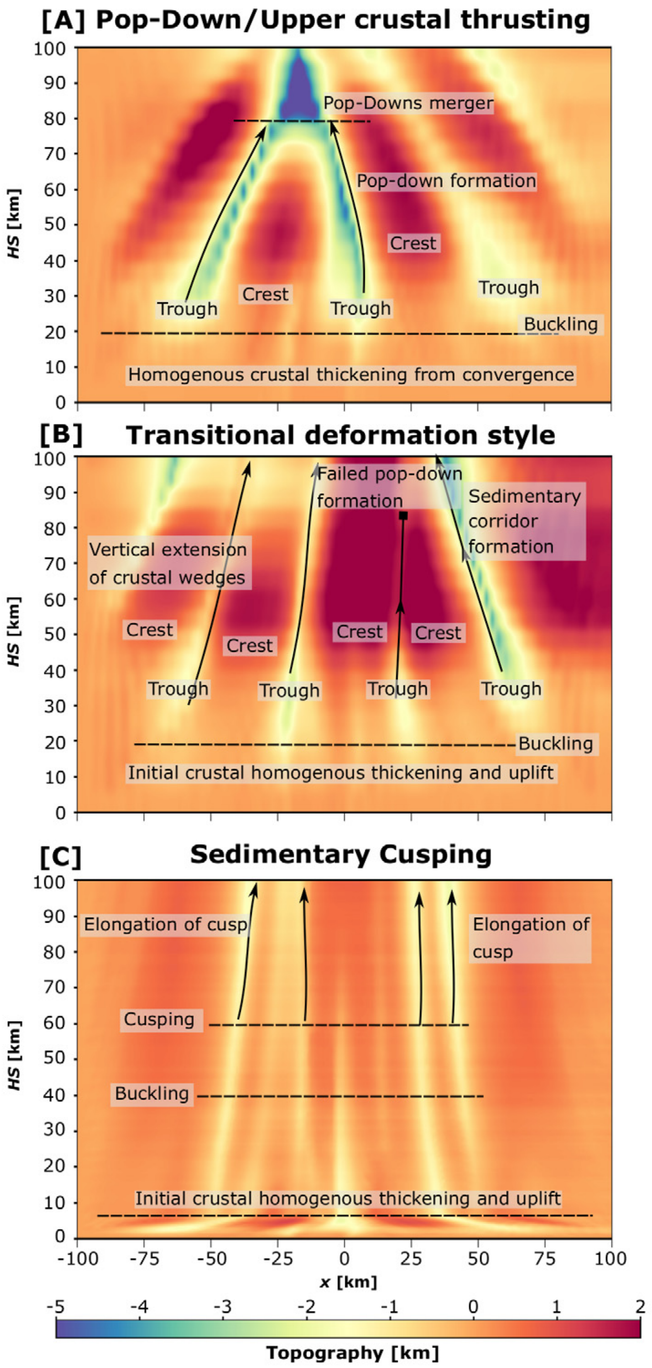

Figure 7: Topography evolution as a function of horizontal shortening for the three tectonic end members. (A) Pop-downs and upper crustal thrusting, (B) transitional deformation style, and (C) sedimentary cusping.

Figure 7: Topography evolution as a function of horizontal shortening for the three tectonic end members. (A) Pop-downs and upper crustal thrusting, (B) transitional deformation style, and (C) sedimentary cusping.

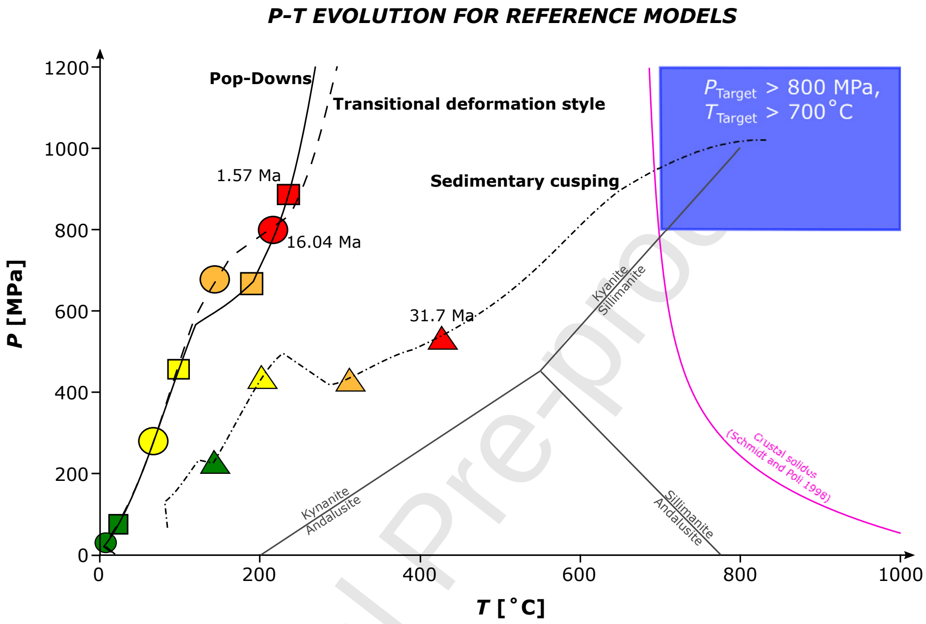

Figure 8: *P-T-t* evolution for the three model end members until *HS* = 140 km. Coloured squares (Pop-downs), circles (transitional deformation style), and triangles (sedimentary cusping) represent increasing horizontal shortening (green = 40 km, yellow = 60 km, orange = 80 km, and red = 100 km). The location of the alumino-silicate triple point is from Holdaway (1971) and Pattison (1992). The blue shaded box represents the upper bounds of the *P-T* targets for the Hearne Craton (P_{Target} = 800 MPa, T_{Target} = 700°C). The solid pink line indicates the crustal solidus curve from Schmidt and Poli (1998).

Figure 8: P-T-t evolution for the three model end members until $HS = 140$ km. Coloured squares (Pop-downs), circles (transitional deformation style), and triangles (sedimentary cusping) represent increasing horizontal shortening (green = 40 km, yellow = 60 km, orange = 80 km, and red = 100 km). The location of the alumino-silicate triple point is from Holdaway (1971) and Pattison (1992). The blue shaded box represents the upper bounds of the P-T targets for the Hearne Craton ($P_{\mathrm{Target}} = 800$ MPa, $T_{\mathrm{Target}} = 700$ °C). The solid pink line indicates the crustal solidus curve from Schmidt and Poli (1998).

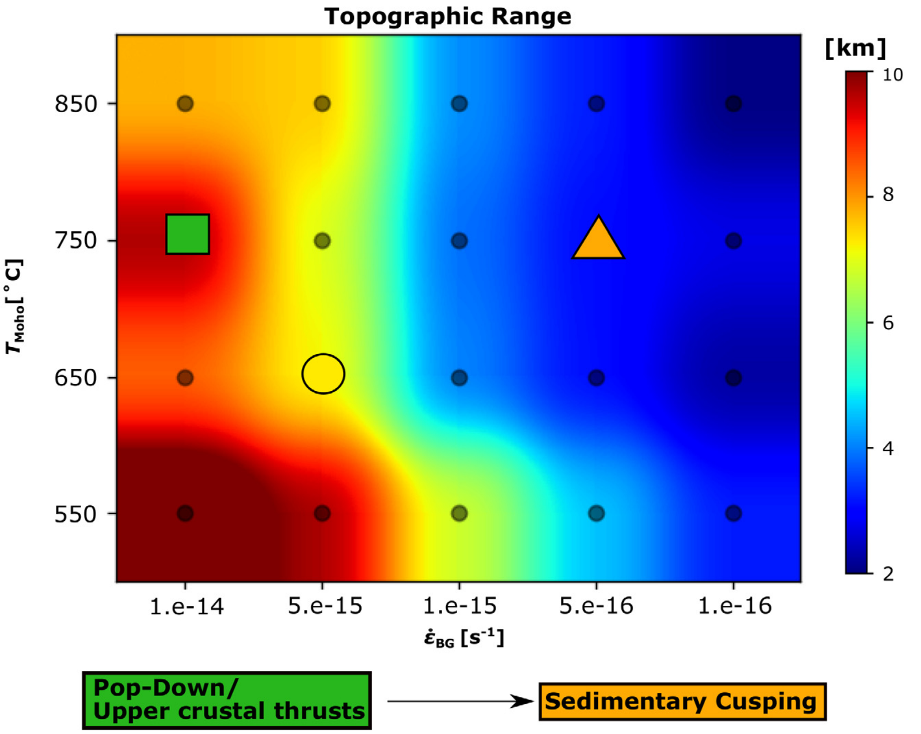

Figure 9: Maximum topographic range obtained from our parametric study. Topographic range is defined by range between the maximum and minimum values obtained until 50% shortening. Refer to Fig. 3A for the transition between different styles of deformation. Dots represent performed experiments.

Figure 9: Maximum topographic range obtained from our parametric study. Topographic range is defined by range between the maximum and minimum values obtained until 50% shortening. Refer to Fig. 3A for the transition between different styles of deformation. Dots represent performed experiments.

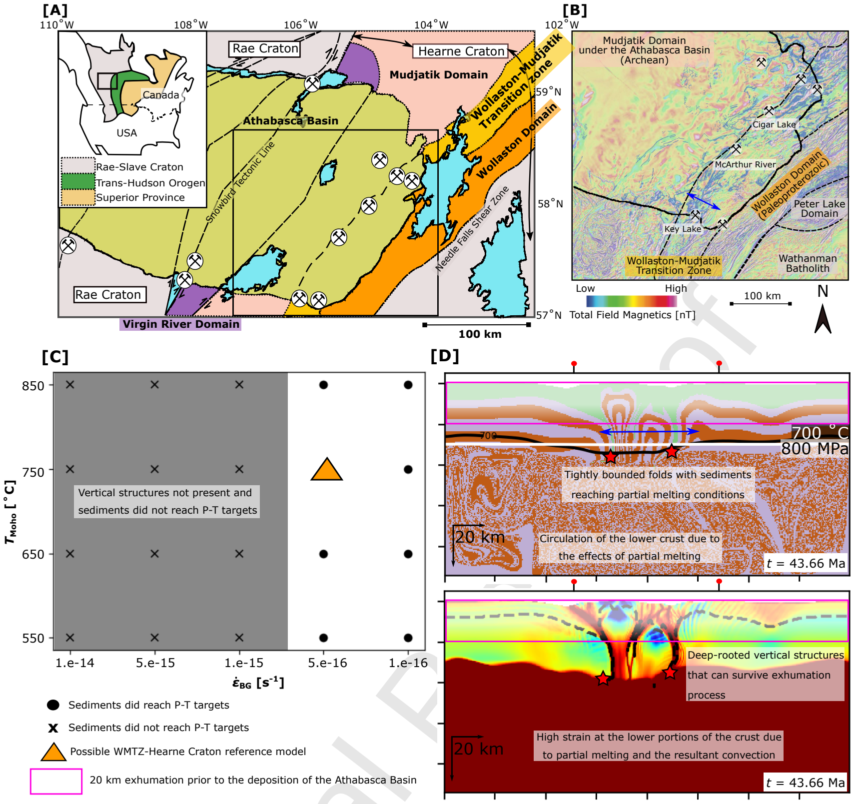

Figure 10: (A) Generalised tectonic domain map of the Hearne-Rae Craton, modified from Alexandre et al. (2007) and Annesley et al. (2005), with several named tectonic lines. (B) Composite aeromagnetic and electromagnetic field map. The blue lines indicate interpreted graphitic conductors, provided by Orano Canada Inc. (C) Comparison of modelling results and the constraints of the study area in which 8 out of 20 models meet the requirements. A possible WMTZ-Hearne Craton reference model is highlighted by an orange triangle, which corresponds to the sedimentary cusping model example in Fig. 6. (D) The reference model with the lithosphere at a higher shortened state (*HS* ~ 133 km), showing the morphological (top) and accumulated strain plots (bottom). To compare the tectonic setting leading to the Athabasca Basin, a distributed erosion of 20 km is removed to ascertain the survival of these deep-seated structures. Blue bi-directional arrows in (B) and (D) show that the first-order structural features are comparable.

Figure 10: (A) Generalised tectonic domain map of the Hearne-Rae Craton, modified from Alexandre et al. (2007) and Annesley et al. (2005), with several named tectonic lines. (B) Composite aeromagnetic and electromagnetic field map. The blue lines indicate interpreted graphitic conductors, provided by Orano Canada Inc. (C) Comparison of modelling results and the constraints of the study area in which 8 out of 20 models meet the requirements. A possible WMTZ-Hearne Craton reference model is highlighted by an orange triangle, which corresponds to the sedimentary cusping model example in Fig. 6. (D) The reference model with the lithosphere at a higher shortened state ($HS \sim 133$ km), showing the morphological (top) and accumulated strain plots (bottom). To compare the tectonic setting leading to the Athabasca Basin, a distributed erosion of 20 km is removed to ascertain the survival of these deep-seated structures. Blue bi-directional arrows in (B) and (D) show that the first-order structural features are comparable.

Thermo-mechanical parametric study of T_{Moho} and $\dot{\varepsilon}_{\mathrm{BG}}$

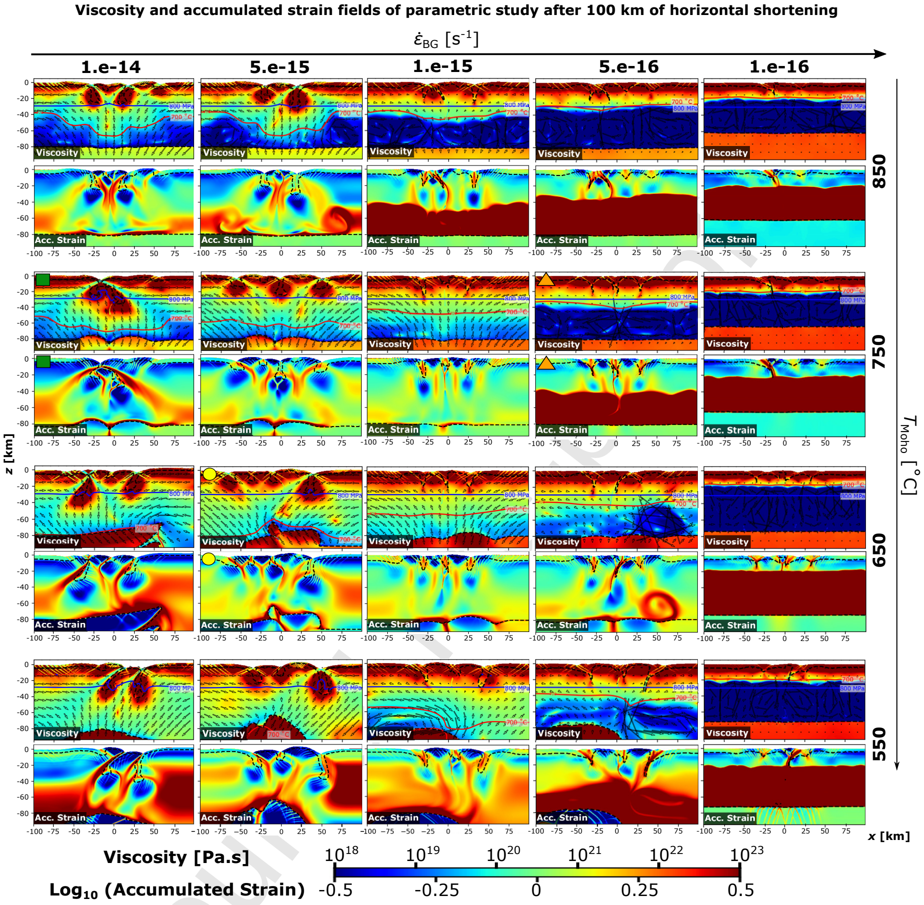
Viscosity and accumulated strain fields of parametric study after 100 km of horizontal shortening

Appendix 1: Snapshots of each model (showing viscosity and accumulated strain fields) after 100 km of horizontal shortening or when the state of deformation has remained unchanged for more than 200 time steps. Dashed lines represent the outline of the sedimentary layer and the Moho. The three reference models (green box, yellow circle, and orange triangle) were shown and discussed in detail within the text, referring to their respective deformation evolutions in Figs. 3 to 8.

Appendix A: Snapshots of each model (showing viscosity and accumulated strain fields) after 100 km of horizontal shortening or when the state of deformation has remained unchanged for more than 200 time steps. Dashed lines represent the outline of the sedimentary layer and the Moho. The three reference models (green box, yellow circle, and orange triangle) were shown and discussed in detail within the text, referring to their respective deformation evolutions in Figs. 3 to 8.

Highlights

- Deformation styles of the lithosphere are controlled by the magnitude of the strain rates.
- High strain rates favour the formation of pop-downs structures and shear zones.
- Low strain rates favour the formation of vertical structures.
- Sedimentary cusping mechanism explains the vertical structures at the Wollaston-Mudjatik Transition zone.
- These vertical structures constitute places for future thermal-fluid convection processes.

[A] Tectonics of hot lithospheres (Ancient tectonics)

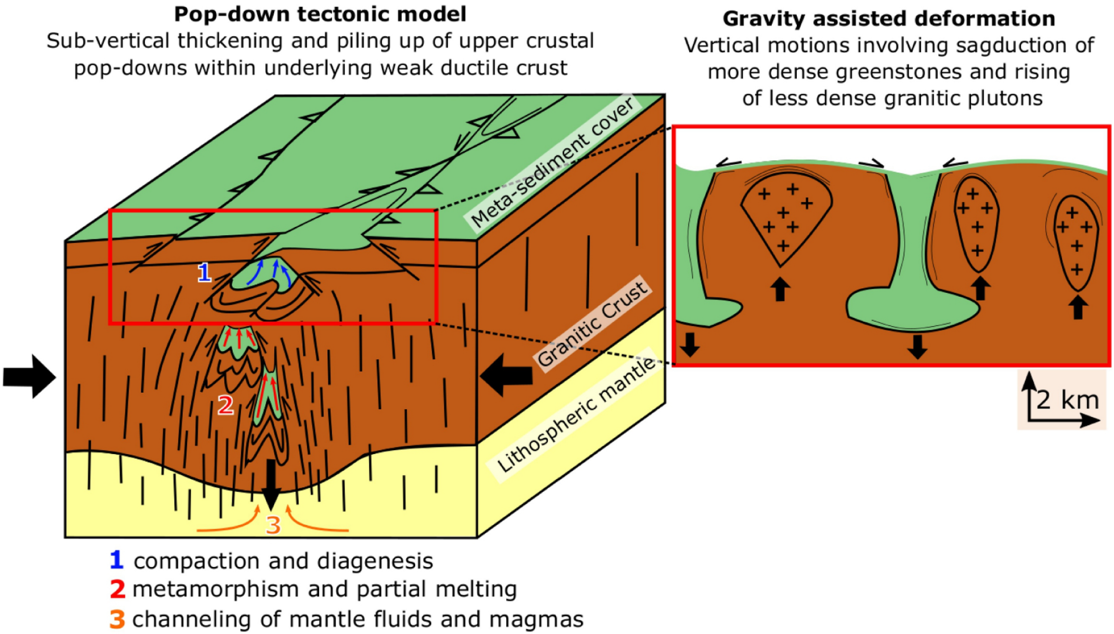

[B] Tectonics of cold lithospheres (Modern tectonics)

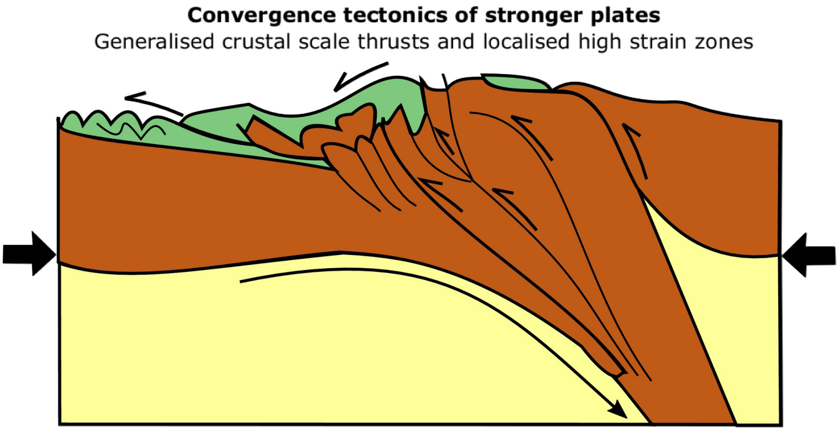

Figure 1

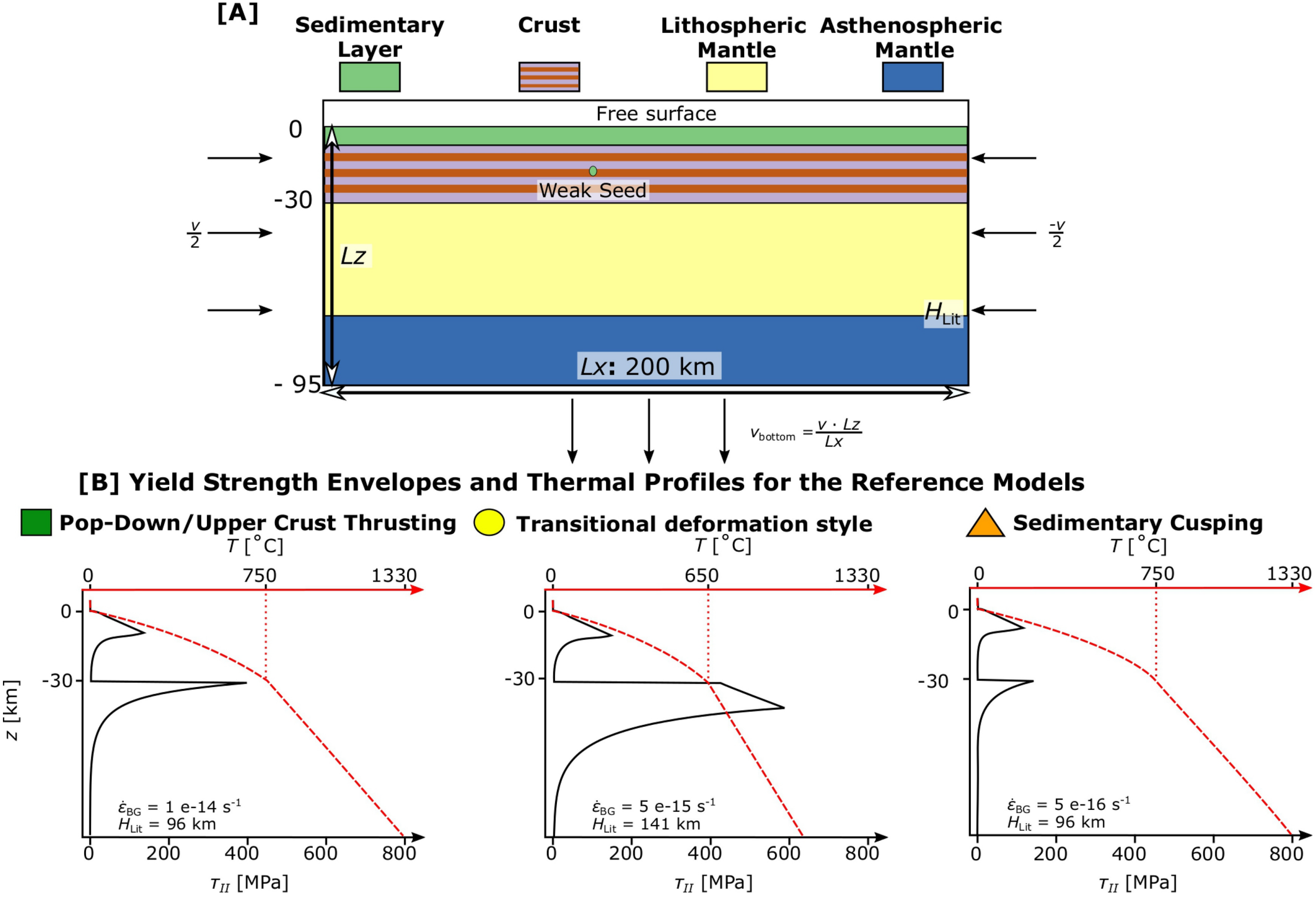
[A]
Sedimentary Layer
Crust
Lithospheric Mantle
Asthenospheric Mantle
Free surface
0
-30
- 95
Weak Seed
$\frac{v}{2}$
$\frac{-v}{2}$
Lz
H_{Lit}
Lx: 200 km
$v_{\mathrm{bottom}} = \frac{v \cdot Lz}{Lx}$
[B] Yield Strength Envelopes and Thermal Profiles for the Reference Models
Pop-Down/Upper Crust Thrusting
Transitional deformation style
Sedimentary Cusping
T [°C]
0
750
650
1330
z [km]
-30
$\dot{\varepsilon}_{\mathrm{BG}}$ = 1 e-14 s^{-1}
H_{Lit} = 96 km
$\dot{\varepsilon}_{\mathrm{BG}}$ = 5 e-15 s^{-1}
H_{Lit} = 141 km
$\dot{\varepsilon}_{\mathrm{BG}}$ = 5 e-16 s^{-1}
H_{Lit} = 96 km
0
200
400
600
800
τ_{II} [MPa]

Figure 2

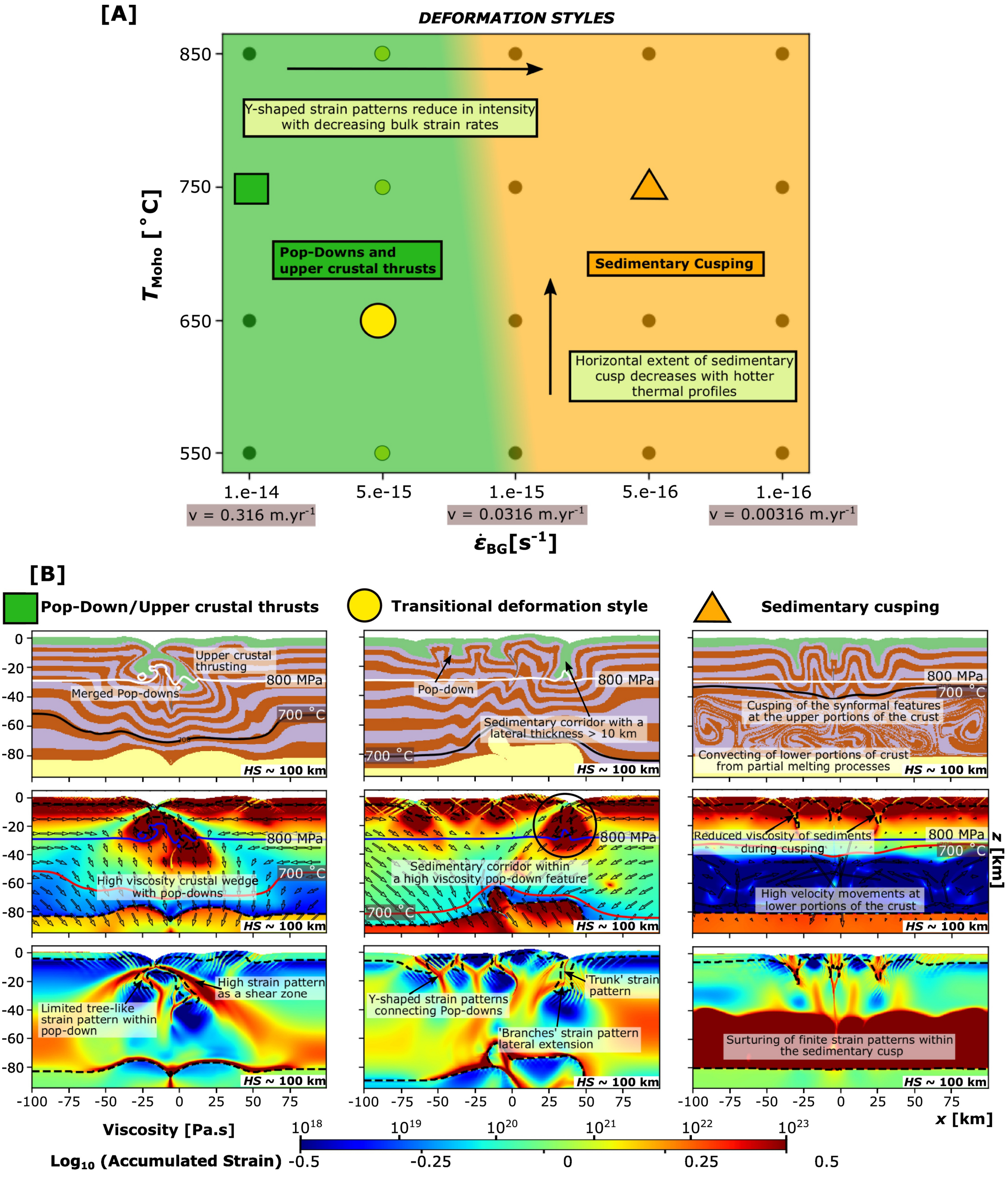
[A]
DEFORMATION STYLES
T_{Moho} [°C]
850
750
650
550
Y-shaped strain patterns reduce in intensity with decreasing bulk strain rates
Pop-Downs and upper crustal thrusts
Sedimentary Cusping
Horizontal extent of sedimentary cusp decreases with hotter thermal profiles
1.e-14
5.e-15
1.e-15
5.e-16
1.e-16
v = 0.316 m.yr-1
v = 0.0316 m.yr-1
v = 0.00316 m.yr-1
$\dot{\varepsilon}_{BG}[s^{-1}]$
[B]
Pop-Down/Upper crustal thrusts
Transitional deformation style
Sedimentary cusping
Upper crustal thrusting
800 MPa
Merged Pop-downs
700 °C
Pop-down
Sedimentary corridor with a lateral thickness > 10 km
Cusping of the synformal features at the upper portions of the crust
Convecting of lower portions of crust from partial melting processes
HS ~ 100 km
High viscosity crustal wedge with pop-downs
Sedimentary corridor within a high viscosity pop-down feature
Reduced viscosity of sediments during cusping
High velocity movements at lower portions of the crust
High strain pattern as a shear zone
Limited tree-like strain pattern within pop-down
Y-shaped strain patterns connecting Pop-downs
'Trunk' strain pattern
'Branches' strain pattern lateral extension
Surturing of finite strain patterns within the sedimentary cusp
z [km]
0
-20
-40
-60
-80
-100
-75
-50
-25
0
25
50
75
x [km]
Viscosity [Pa.s]
10^{18}
10^{19}
10^{20}
10^{21}
10^{22}
10^{23}
Log_{10} (Accumulated Strain)
-0.5
-0.25
0
0.25
0.5

Figure 3

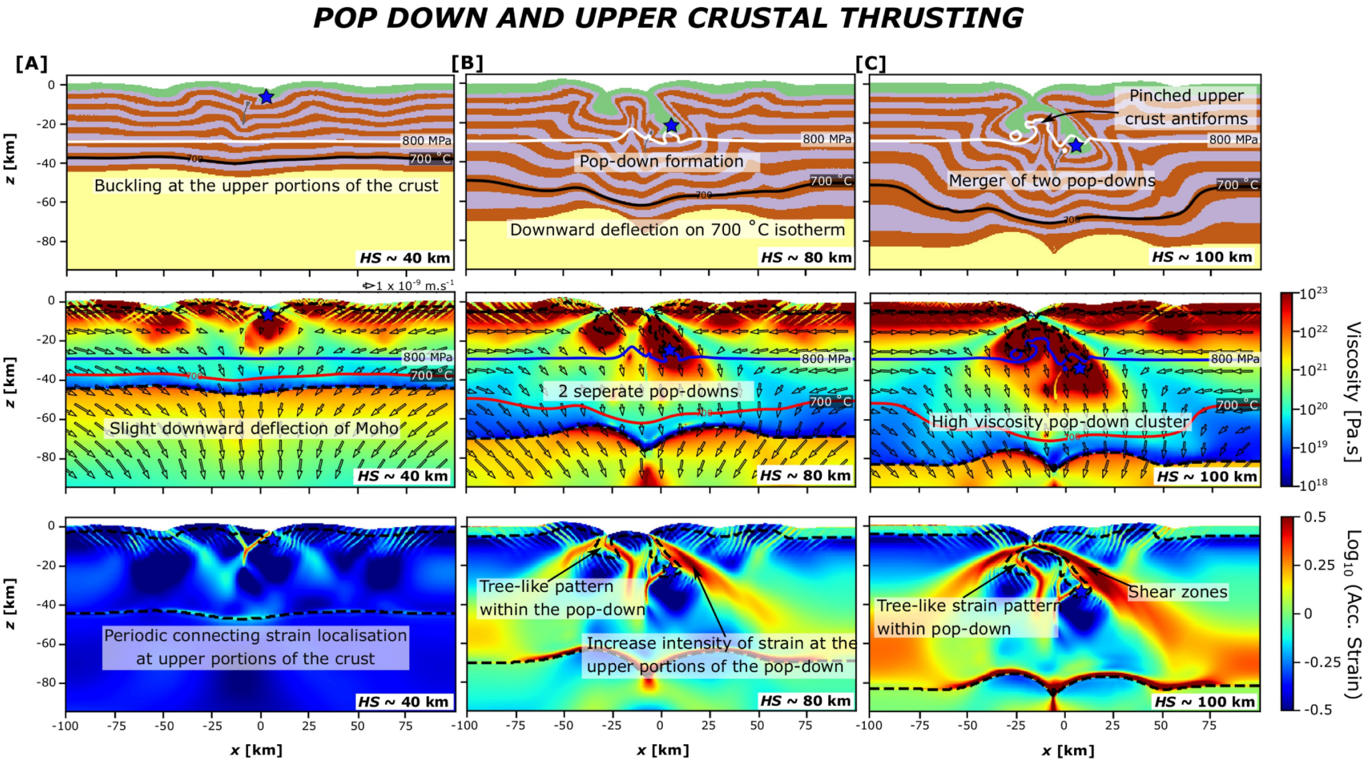
POP DOWN AND UPPER CRUSTAL THRUSTING
[A]
[B]
[C]
z [km]
0
-20
-40
-60
-80
800 MPa
700 °C
700
Buckling at the upper portions of the crust
HS ~ 40 km
Pop-down formation
Downward deflection on 700 °C isotherm
HS ~ 80 km
Pinched upper crust antiforms
Merger of two pop-downs
HS ~ 100 km
1 x 10⁻⁹ m.s⁻¹
Slight downward deflection of Moho
2 seperate pop-downs
High viscosity pop-down cluster
Viscosity [Pa.s]
10²³
10²²
10²¹
10²⁰
10¹⁹
10¹⁸
Periodic connecting strain localisation at upper portions of the crust
Tree-like pattern within the pop-down
Increase intensity of strain at the upper portions of the pop-down
Tree-like strain pattern within pop-down
Shear zones
Log₁₀ (Acc. Strain)
0.5
0.25
0
-0.25
-0.5
-100
-75
-50
-25
0
25
50
75
x [km]

Figure 4

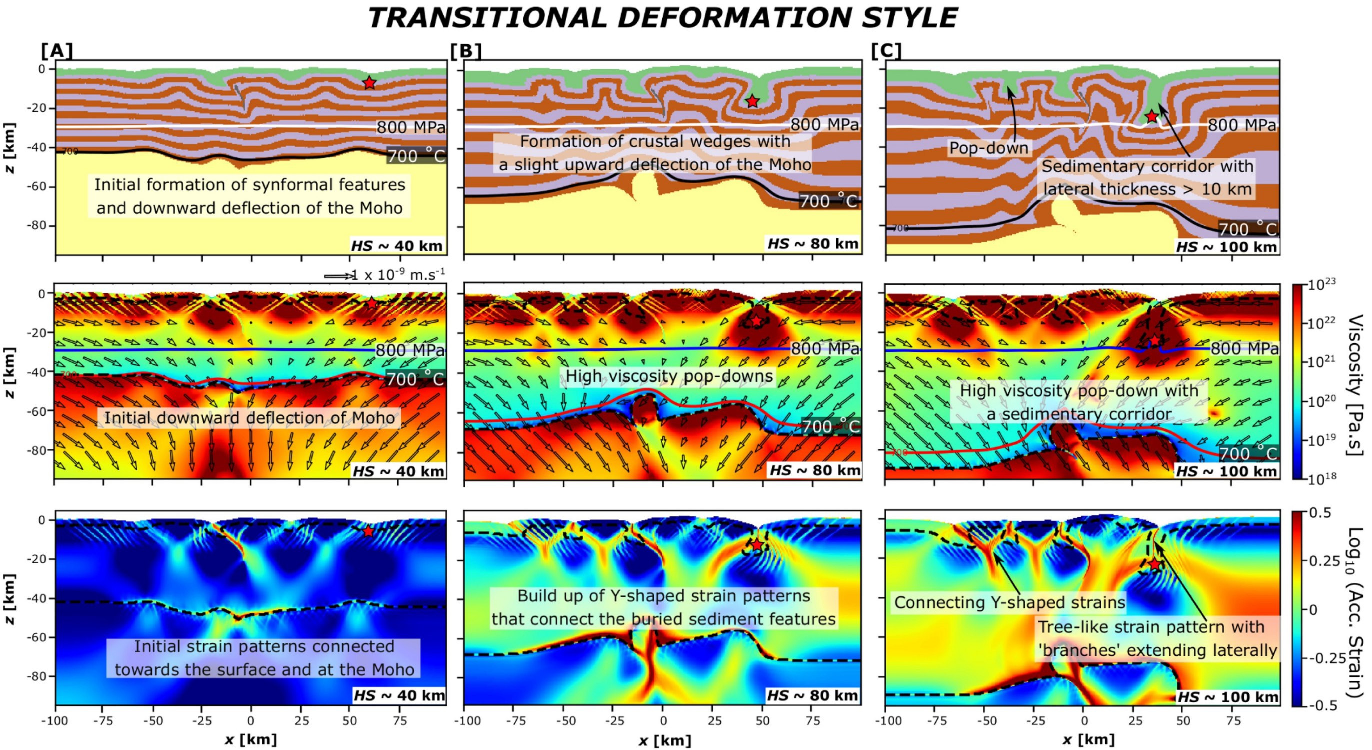
TRANSITIONAL DEFORMATION STYLE
[A]
[B]
[C]
z [km]
x [km]
800 MPa
700 °C
Initial formation of synformal features and downward deflection of the Moho
Formation of crustal wedges with a slight upward deflection of the Moho
Pop-down
Sedimentary corridor with lateral thickness > 10 km
HS ~ 40 km
HS ~ 80 km
HS ~ 100 km
1 x 10^{-9} m.s^{-1}
Initial downward deflection of Moho
High viscosity pop-downs
High viscosity pop-down with a sedimentary corridor
Viscosity [Pa.s]
10^{18}
10^{19}
10^{20}
10^{21}
10^{22}
10^{23}
Initial strain patterns connected towards the surface and at the Moho
Build up of Y-shaped strain patterns that connect the buried sediment features
Connecting Y-shaped strains
Tree-like strain pattern with 'branches' extending laterally
Log$_{10}$ (Acc. Strain)
-0.5
-0.25
0
0.25
0.5
-100
-75
-50
-25
0
25
50
75
-20
-40
-60
-80

Figure 5

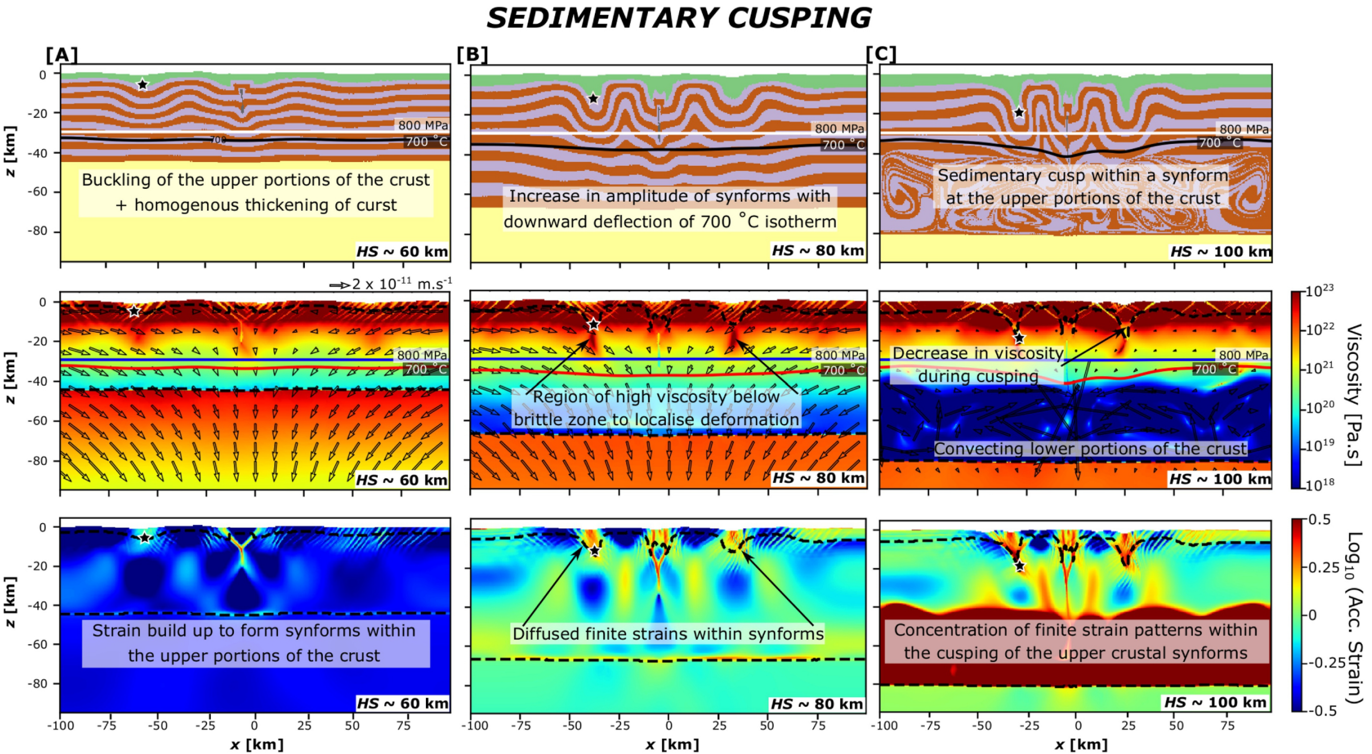
SEDIMENTARY CUSPING
[A]
[B]
[C]
z [km]
0
-20
-40
-60
-80
800 MPa
700 °C
700
Buckling of the upper portions of the crust + homogenous thickening of curst
Increase in amplitude of synforms with downward deflection of 700 °C isotherm
Sedimentary cusp within a synform at the upper portions of the crust
HS ~ 60 km
HS ~ 80 km
HS ~ 100 km
2 x 10^{-11} m.s^{-1}
Region of high viscosity below brittle zone to localise deformation
Decrease in viscosity during cusping
Convecting lower portions of the crust
Viscosity [Pa.s]
10^{23}
10^{22}
10^{21}
10^{20}
10^{19}
10^{18}
Strain build up to form synforms within the upper portions of the crust
Diffused finite strains within synforms
Concentration of finite strain patterns within the cusping of the upper crustal synforms
Log$_{10}$ (Acc. Strain)
0.5
0.25
0
-0.25
-0.5
-100
-75
-50
-25
0
25
50
75
x [km]

Figure 6

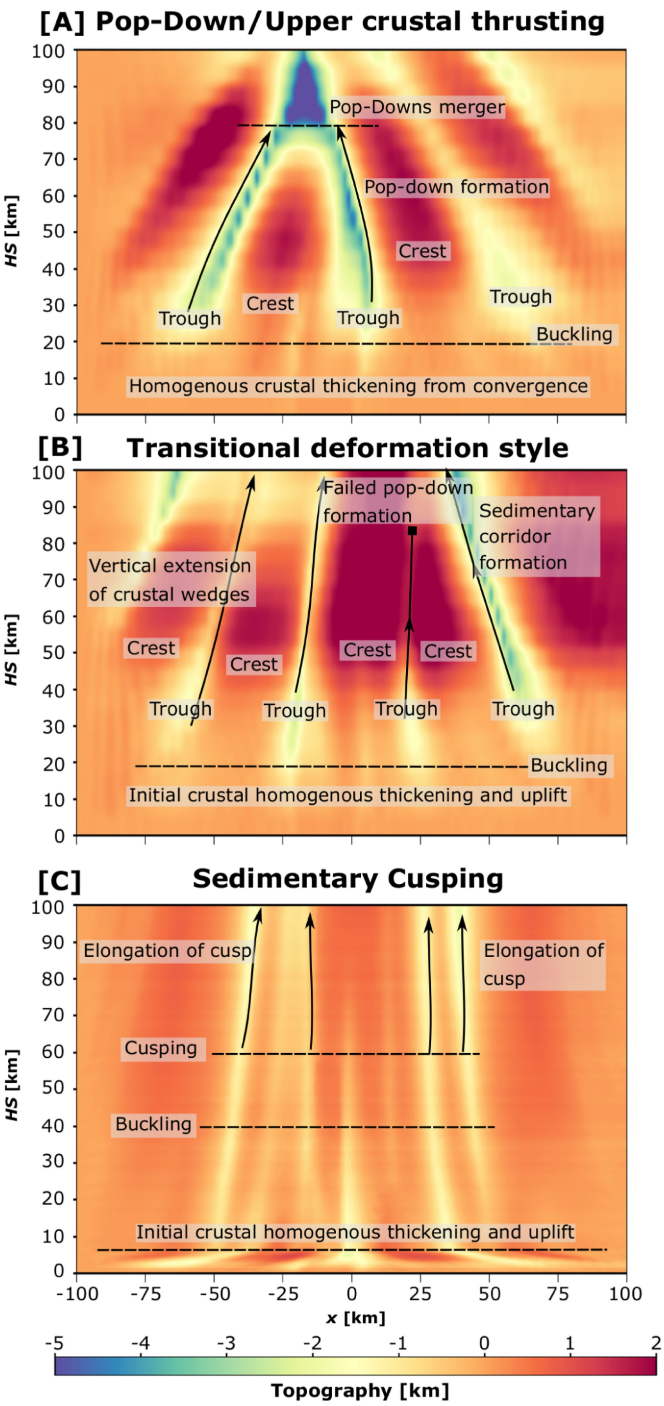

[A] Pop-Down/Upper crustal thrusting
Pop-Downs merger
Pop-down formation
Crest
Trough
Crest
Trough
Trough
Buckling
Homogenous crustal thickening from convergence
[B] Transitional deformation style
Failed pop-down formation
Sedimentary corridor formation
Vertical extension of crustal wedges
Crest
Crest
Crest
Crest
Trough
Trough
Trough
Trough
Buckling
Initial crustal homogenous thickening and uplift
[C] Sedimentary Cusping
Elongation of cusp
Elongation of cusp
Cusping
Buckling
Initial crustal homogenous thickening and uplift
HS [km]
0
10
20
30
40
50
60
70
80
90
100
x [km]
-100
-75
-50
-25
0
25
50
75
100
Topography [km]
-5
-4
-3
-2
-1
0
1
2

Figure 7

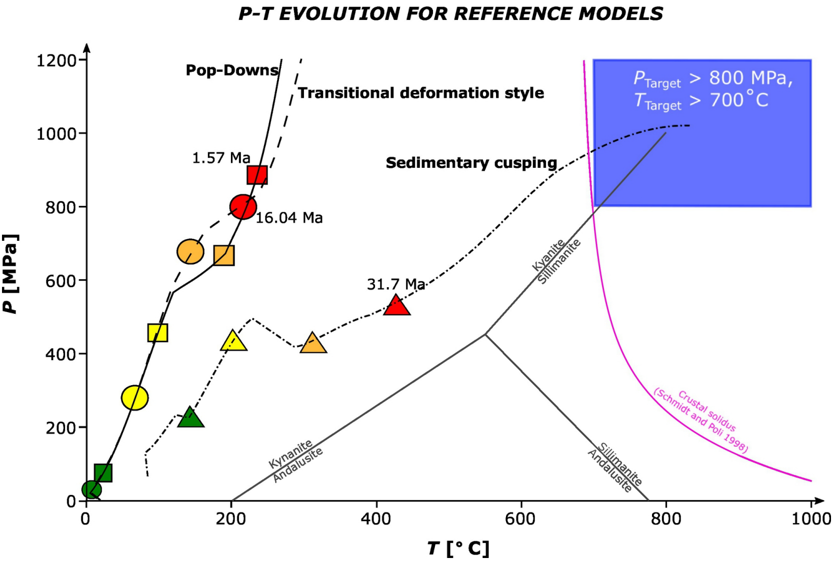
P-T EVOLUTION FOR REFERENCE MODELS
P [MPa]
T [° C]
0
200
400
600
800
1000
1200
Pop-Downs
Transitional deformation style
Sedimentary cusping
1.57 Ma
16.04 Ma
31.7 Ma
P_{Target} > 800 MPa,
T_{Target} > 700 °C
Kyanite
Sillimanite
Kynanite
Andalusite
Sillimanite
Andalusite
Crustal solidus
(Schmidt and Poli 1998)

Figure 8

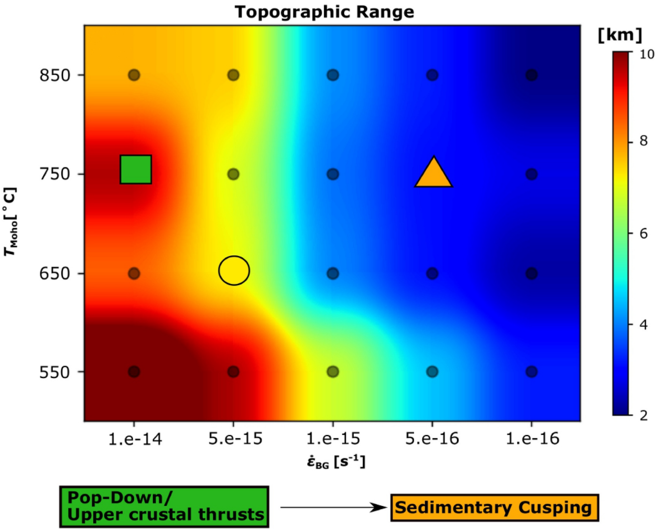
Topographic Range
[km]
10
8
6
4
2
850
750
650
550
T_Moho [°C]
1.e-14
5.e-15
1.e-15
5.e-16
1.e-16
ε̇_BG [s^-1]
Pop-Down/
Upper crustal thrusts
Sedimentary Cusping

Figure 9

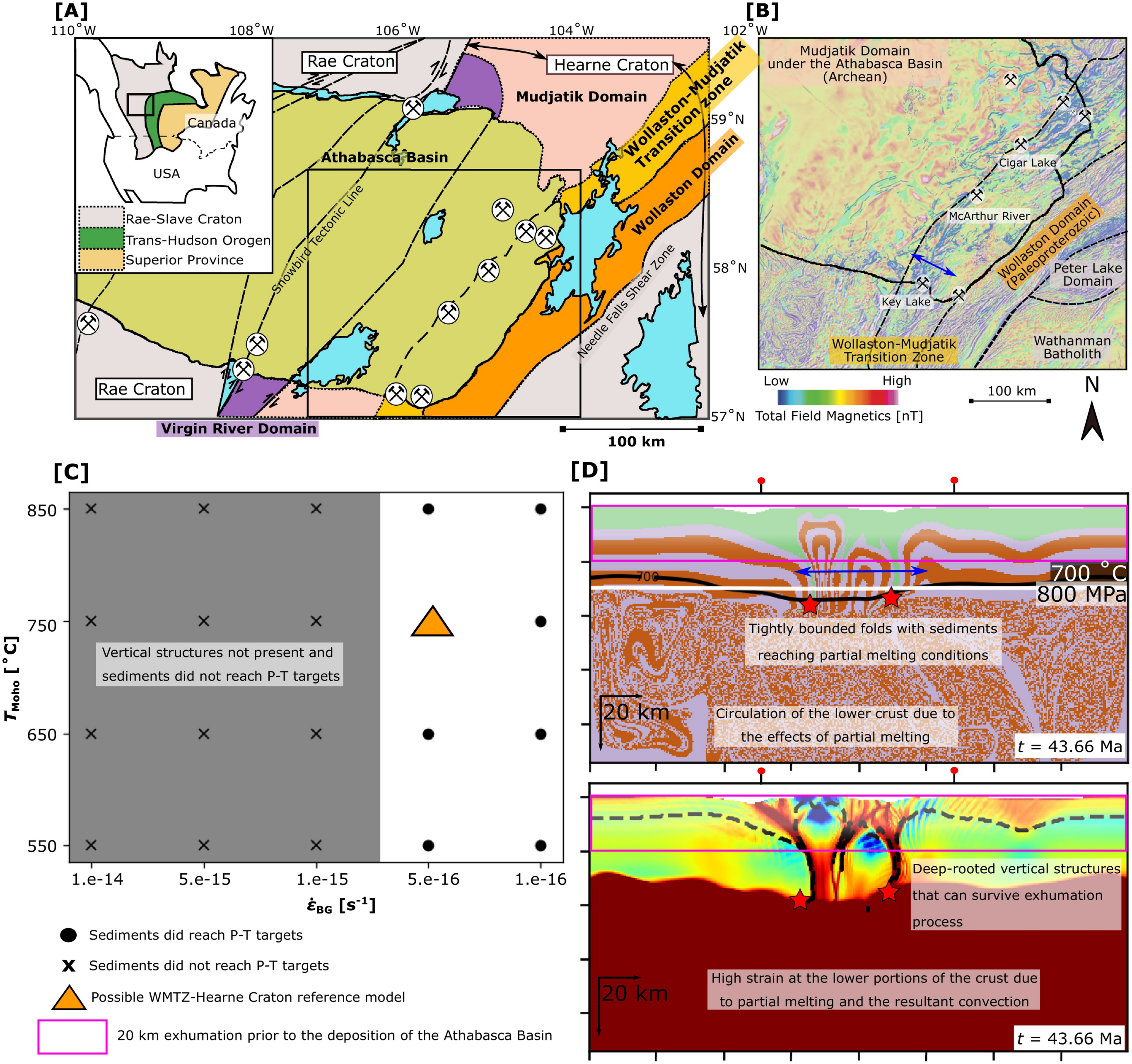
[A]
110°W
108°W
106°W
104°W
102°W
59°N
58°N
57°N
Rae Craton
Hearne Craton
Mudjatik Domain
Wollaston-Mudjatik Transition zone
Wollaston Domain
Athabasca Basin
Snowbird Tectonic Line
Needle Falls Shear Zone
Rae Craton
Virgin River Domain
100 km
Canada
USA
Rae-Slave Craton
Trans-Hudson Orogen
Superior Province
[B]
Mudjatik Domain under the Athabasca Basin (Archean)
Cigar Lake
McArthur River
Key Lake
Wollaston Domain (Paleoproterozoic)
Peter Lake Domain
Wollaston-Mudjatik Transition Zone
Wathanman Batholith
Low
High
Total Field Magnetics [nT]
100 km
N
[C]
T_{Moho} [°C]
850
750
650
550
1.e-14
5.e-15
1.e-15
5.e-16
1.e-16
$\dot{\varepsilon}_{BG}$ [s^{-1}]
Vertical structures not present and sediments did not reach P-T targets
● Sediments did reach P-T targets
× Sediments did not reach P-T targets
▲ Possible WMTZ-Hearne Craton reference model
▭ 20 km exhumation prior to the deposition of the Athabasca Basin
[D]
700
700 °C
800 MPa
Tightly bounded folds with sediments reaching partial melting conditions
20 km
Circulation of the lower crust due to the effects of partial melting
t = 43.66 Ma
Deep-rooted vertical structures that can survive exhumation process
20 km
High strain at the lower portions of the crust due to partial melting and the resultant convection
t = 43.66 Ma

Figure 10